Monthly Notices of the ROYAL ASTRONOMICAL SOCIETY

MNRAS **504,** 3265–3283 (2021) doi:10.1093/mnras/stab998
Advance Access publication 2021 April 10

The AGNIFS survey: distribution and excitation of the hot molecular and ionized gas in the inner kpc of nearby AGN hosts

R. A. Riffel [1]★ T. Storchi-Bergmann,[2] R. Riffel [2] M. Bianchin,[1] N. L. Zakamska [3] D. Ruschel-Dutra,[4] A. J. Schönell,[5] D. J. Rosario,[6] A. Rodriguez-Ardila,[7] T. C. Fischer,[8] R. I. Davies [9] N. Z. Dametto [10] L. G. Dahmer-Hahn,[7] D. M. Crenshaw,[11] L. Burtscher[12] and M. C. Bentz[11]

[1]*Departamento de Física, Centro de Ciências Naturais e Exatas, Universidade Federal de Santa Maria, 97105-900 Santa Maria, RS, Brazil*
[2]*Instituto de Física, Universidade Federal do Rio Grande do Sul, Av. Bento Gonçalves 9500, 91501-970 Porto Alegre, RS, Brazil*
[3]*Department of Physics & Astronomy, Johns Hopkins University, Bloomberg Center, 3400 N. Charles St, Baltimore, MD 21218, USA*
[4]*Departamento de Física, Universidade Federal de Santa Catarina, P.O. Box 476, 88040-900 Florianópolis, SC, Brazil*
[5]*Instituto Federal de Educação, Ciência e Tecnologia Farroupilha, BR287, km 360, Estrada do Chapadão, 97760-000 Jaguari - RS, Brazil*
[6]*Centre for Extragalactic Astronomy, Department of Physics, Durham University, South Road, DH1 3LE Durham, UK*
[7]*Laboratório Nacional de Astrofísica. Rua dos Estados Unidos, 154, CEP 37504-364 Itajubá, MG, Brazil*
[8]*AURA for ESA, Space Telescope Science Institute, 3700 San Martin Drive, Baltimore, MD 21218, USA*
[9]*Max-Planck-Institut für Extraterrestrische Physik, Postfach 1312, D-85741 Garching, Germany*
[10]*Centro de Astronomía (CITEVA), Universidad de Antofagasta, Avenida Angamos 601, 02800 Antofagasta, Chile*
[11]*Department of Physics and Astronomy, Georgia State University, 25 Park Place, Suite 605, Atlanta, GA 30303, USA*
[12]*Leiden Observatory, Leiden University, PO Box 9513, NL-2300 RA, Leiden, the Netherlands*

Accepted 2021 April 5. Received 2021 March 8; in original form 2020 October 20

ABSTRACT

We use the Gemini NIFS instrument to map the H_2 2.1218 μm and Brγ flux distributions in the inner 0.04–2 kpc of a sample of 36 nearby active galaxies ($0.001 \lesssim z \lesssim 0.056$) at spatial resolutions from 4 to 250 pc. We find extended emission in 34 galaxies. In ∼55 per cent of them, the emission in both lines is most extended along the galaxy major axis, while in the other 45 per cent the extent follows a distinct orientation. The emission of H_2 is less concentrated than that of Brγ, presenting a radius that contains half of the flux 60 per cent greater, on average. The H_2 emission is driven by thermal processes – X-ray heating and shocks – at most locations for all galaxies, where $0.4 < H_2/Br\gamma < 6$. For regions where $H_2/Br\gamma > 6$ (seen in 40 per cent of the galaxies), shocks are the main H_2 excitation mechanism, while in regions with $H_2/Br\gamma < 0.4$ (25 per cent of the sample) the H_2 emission is produced by fluorescence. The only difference we found between type 1 and type 2 active galactic nucleus (AGN) was in the nuclear emission-line equivalent widths that are smaller in type 1 than in type 2 due to a larger contribution to the continuum from the hot dusty torus in the former. The gas masses in the inner 125 pc radius are in the range 10^1-10^4 $M_\odot$ for the hot H_2 and 10^3-10^6 $M_\odot$ for the ionized gas and would be enough to power the AGN in our sample for 10^5-10^8 yr at their current accretion rates.

Key words: techniques: imaging spectroscopy – galaxies: active – galaxies: ISM – galaxies: Seyfert.

1 INTRODUCTION

The presence of a gas reservoir in the inner few tens of parsecs of galaxies is a necessary requirement to trigger an active galactic nucleus (AGN) and/or a nuclear starburst. Understanding the origin of the gas emission at these scales is critical to investigate the role of AGN and star formation (SF) feedback in galaxy evolution. The cold molecular gas is the raw fuel of SF in the central region of galaxies and AGN, while the ionized gas is usually observed as a consequence of SF and nuclear activity. The ionized gas is easier to trace, since the strongest emission lines are observed in the optical region. These emission lines are good tracers of many galactic components, such as discs, outflows, and AGN (e.g. Ricci, Steiner & Menezes 2014).

However, there are no strong emission lines of molecular gas in the optical. For this reason, most studies of molecular hydrogen distribution and kinematics usually use other molecules as its tracer, such as the CO emission at submillimetre wavelengths. These studies have found that there are two main classes of galaxies regarding their molecular gas distribution: a starburst one, where the molecular gas distribution is very compact with short consumption times (10^7–10^8 yr), and a quiescent one, with the gas distributed in extended discs and longer consumption times (∼10^9 yr) (Daddi et al. 2010; Genzel et al. 2010; Sargent et al. 2014; Silverman et al. 2015). In order to properly compare ionized and molecular gas distributions, however, it is ideal that they are observed in the same wavelength range and with the same spatial resolution.

In the near-infrared (hereafter near-IR) both gas phases, hot molecular and ionized, can be observed simultaneously. In particular, the *K*-band spectra of galaxies include ro-vibrational emission lines

★ E-mail: rogemar@ufsm.br

from the H_2, tracing the hot molecular gas that represents only a small fraction of the total molecular gas, and the hydrogen recombination line Brγ, a tracer of the ionized gas (e.g Riffel, Rodríguez-Ardila & Pastoriza 2006). Physically motivated models (Hopkins & Quataert 2010) show that the relevant feeding processes occur within the inner kiloparsec, which can only be resolved in nearby galaxies. Near-IR integral field spectroscopy (IFS) on 8–10 m telescopes is a unique tool to investigate the distribution and kinematics of the molecular and ionized gas at spatial resolutions of 10–100 pc providing observational constraints to better understand the AGN feeding and feedback processes. Such constraints are fundamental ingredients of theoretical models and numerical simulations of galaxy evolution aimed to understand the co-evolution of AGN and their host galaxies (Kormendy & Ho 2013; Heckman & Best 2014; Harrison 2017; Harrison et al. 2018; Storchi-Bergmann & Schnorr-Müller 2019).

The near-IR emission of molecular and ionized gas have been investigated over the years using both long slit spectroscopy (e.g. Rodríguez-Ardila et al. 2004; Rodríguez-Ardila, Riffel & Pastoriza 2005; Riffel et al. 2006, 2013a; Lamperti et al. 2017) and spatially resolved observations (e.g. Riffel et al. 2008, 2020; Davies et al. 2009; Hicks et al. 2009; Storchi-Bergmann et al. 2009; Mazzalay et al. 2013; Scharwächter et al. 2013; Barbosa et al. 2014; Durré & Mould 2014, 2018; Schönell et al. 2014, 2017; Diniz et al. 2015; Fischer et al. 2017; Husemann et al. 2019; Rosario et al. 2019; Shimizu et al. 2019). In most cases, the hot molecular and ionized gas show distinct flux distributions and kinematics, with the H_2 more restricted to the galaxy plane following circular rotation and the ionized gas showing more collimated emission and contribution of non-circular motions. However, in few cases, hot molecular outflows are also observed (e.g. Davies et al. 2014; Fischer et al. 2017; May & Steiner 2017; Gnilka et al. 2020; May et al. 2020; Riffel et al. 2020). These results, combined with the fact that the ionized gas is usually associated with higher temperatures when compared to the molecular gas, has led Storchi-Bergmann et al. (2009) to suggest that the molecular gas is a better tracer of AGN feeding, whereas the ionized gas is a better tracer of AGN feedback. While the studies above have addressed the origin, morphology, and amount of molecular gas in individual sources, it is now necessary to trace a more complete picture of the subject from a statistical point of view. This will allow us to detect common points and differences in order to advance on the knowledge of the origin and black hole feeding mechanisms in AGN and galaxies overall.

A few studies using near-IR IFS on larger samples have also been carried out, as for example those of the AGNIFS survey (Riffel et al. 2017, 2018; Schönell et al. 2019), the Local Luminous AGN with Matched Analogs survey (Davies et al. 2015; Lin et al. 2018; Caglar et al. 2020) and the Keck OSIRIS Nearby AGN survey (Müller-Sánchez et al. 2018b). But so far, the studies based on these surveys were aimed to describe the sample, map its stellar kinematics and nuclear properties of the galaxies, while the origin, amount, and distribution of the hot molecular hydrogen in the inner kiloparsec of nearby AGN are still not properly covered and mapped.

In the present work, we use *K*-band IFS of a sample of 36 AGN of the local Universe, observed with the Gemini Near-infrared Integral Field Spectrograph (NIFS), to map their molecular and ionized gas flux distributions at resolutions ranging from a few pc to ≈250 pc. We investigate the origin of the H_2 emission, derive the H_2 excitation temperature and mass of hot molecular and ionized gas, available to feed the central AGN and SF. This paper is organized as follows: Section 2 presents the sample, observations, and data reduction procedure, Section 3 presents the results, which are discussed in Section 4. We present our conclusions in Section 5. We use a $h = 0.7$, $\Omega_m = 0.3$, and $\Omega_\Lambda = 0.7$ cosmology throughout this paper.

2 THE SAMPLE AND DATA

2.1 The sample

We used the catalog of hard X-ray (14–195 keV) sources detected in the first 105 months of observations of the Swift Burst Alert Telescope (BAT) survey (Oh et al. 2018) to select our parent sample of AGN. The hard X-ray measures direct emission from the AGN and is much less sensitive to obscuration along the line of sight than softer X-ray and optical observations (see Davies et al. 2015, for a discussion about the advantages of using BAT catalogue to select AGN). This sample was cross-correlated with the Gemini Science archive looking for data obtained with the NIFS in the *K* band. We emphasize that just like any other AGN selection method (e.g. based on optical emission lines), our selection criteria may not include all AGN available in the Gemini database. As the aim of this work is to study the hot molecular hydrogen emission from AGN hosts, we limit our search to redshifts $z < 0.12$, for which the H_2 2.1218 μm is still accessible in the *K* band.

We have found NIFS data for 36 galaxies obtained using the K and K_{long} gratings, most of them observed as part of the Brazilian Large Gemini Program NIFS survey of feeding and feedback processes in nearby active galaxies (Riffel et al. 2018). The central wavelengths of the K and K_{long} gratings are 2.20 and 2.30 μm, respectively. For both gratings, the bandwidth is ∼4000 Å and the spectral bin is ∼2.13 Å. Table 1 lists the galaxies of our sample, as well as their morphologies, nuclear activity types, redshifts, hard X-ray luminosities (L_X) obtained from the Swift BAT survey (Oh et al. 2018), Gemini Program ID, exposure time and the full width at half-maximum (FWHM) of the point spread function (PSF) measured from the flux distribution of the telluric standard stars for the type 2 AGN and from the flux distribution of the broad Brγ emission line for the observed type 1 AGN. Although our redshift limit is $z < 0.12$, the most distant galaxy (Cygnus A) we have found in the archive obeying all our criteria has $z \sim 0.056$. Except NGC 1052, all galaxies in our sample are classified as hosting Seyfert nuclei. The nature of LINERs is still not well understood, as similar line ratios can be produced by distinct mechanisms (e.g. AGN, hot low-mass evolved stars and shocks). However, NGC 1052 undoubtedly presents an AGN as indicated by by its optical emission lines (Heckman 1980; Ho et al. 1997; Dahmer-Hahn et al. 2019b), by the detection of a hidden broad line region seen in polarized light that shows a broad Hα component (Barth, Filippenko & Moran 1999) and by its high hard X-ray luminosity, comparable to the luminosities in Seyfert nuclei (Table 1). We divide the sample into type 1 (1–1.5) and type 2 (1.9 and 2), according to the classification in the 105 month BAT catalogue (Oh et al. 2018). The type 1 and type 2 subsamples have the same number (18) of objects.

In Fig. 1, we show the X-ray luminosity and redshift distribution of the galaxies of our sample. We divide the sample into type 1 (blue-dashed line) and type 2 (red-continuous line) as in the Table 1. To test whether the distributions for the type 1 and type 2 are drawn from the same underlying distribution, we use the Kolmogorov–Smirnov (K–S) test and compute the probability of the null hypothesis (P_{KS}). $P_{KS} < 0.05$ implies that the null hypothesis that the two distributions are drawn from the same underlying distribution is rejected at a confidence level of 95 per cent. We find high values of P_{KS} for both L_X ($P_{KS} = 0.75$) and z ($P_{KS} = 0.24$) distributions, meaning that the

Table 1. The sample: (1) Galaxy name. The superscript letter in the name of some galaxies identifies the reference of previously published NIFS *K* band, listed below. All galaxies were observed using AOs, except NGC 1125 and ESO578-G009 (marked with a † symbol). (2) Morphological classification from de Vaucouleurs et al. (1991), (3) Nuclear Activity Classification from Oh et al. (2018). (4) redshift, (5) adopted distance, (6) hard X-ray (14-195 keV) luminosity, (7) Gemini Program ID (prefix: GN-20), (8) Grating used during the observations. The central wavelengths are 2.2 and 2.3 μm for the K and K_{long} (K_l) gratings, respectively. The spectral coverage of both gratings is ∼4000 Å. (9) exposure time, (10) angular resolution, and (11) spatial scale of 1 arcsec projected at the galaxy distance. References to previous works on NIFS data: *a*) Schönell et al. (2019); *b*) Dahmer-Hahn et al. (2019a); *c*) Riffel et al. (2014), *d*) Diniz et al. (2015); *e*) Drehmer et al. (2015); *f*) Ilha, Bianchin & Riffel (2016); *g*) Gnilka et al. (2020); *h*) Riffel et al. (2010b); *i*) Husemann et al. (2019); *j*) Riffel et al. (2020); *k*) Riffel et al. (2008); *l*) Storchi-Bergmann et al. (2009); *m*) Brum et al. (2019); *n*) Schönell et al. (2017); *o*) Riffel, Storchi-Bergmann & Winge (2013b); *p*) Diniz, Riffel & Dors (2018). and *q*) Schönell et al. (2014).

Galaxy	Hubble type	Act. type	z	D (Mpc)	log L_X (erg s^{-1})	Program ID	Grating	Exp. time (s)	$FWHM_{PSF}$ (arcsec)	Scale (pc)
(1)	(2)	(3)	(4)	(5)	(6)	(7)	(8)	(9)	(10)	(11)
				type 2						
NGC 788[a]	SA0/a?(s)	Sy2	0.0136	58.3	43.51	15B-Q-29	K	11 × 400	0.13	282
NGC 1052[b]	E4	LINER	0.0050	21.4	42.24	10B-Q-25	K_l	4 × 600	0.15	103
NGC 1068[c]	(R)SA(rs)b	Sy1.9	0.0038	16.3	42.08	06B-C-9	K	27 × 90	0.11	78
NGC 1125†	(R')SB0/a?(r)	Sy2	0.0109	47.1	42.64	18B-Q-140	K	8 × 450	0.44	228
NGC 1241	SB(rs)b	Sy2	0.0135	57.9	42.68	19A-Q-106	K	6 × 600	0.14	280
NGC 2110[d]	$SAB0^-$	Sy2	0.0078	33.4	43.65	10B-Q-25	K_l	6 × 600	0.15	162
NGC 3393	(R')SB(rs)a?	Sy2	0.0125	53.6	42.98	12A-Q-2	K	4 × 600	0.13	260
NGC 4258[e]	SAB(s)bc	Sy1.9	0.0015	6.4	41.06	07A-Q-25	K	10 × 600	0.20	31
NGC 4388	SA(s)b? edge-on	Sy2	0.0084	36.0	43.64	15A-Q-3	K	2 × 400	0.19	174
NGC 5506[a]	Sa pec edge-on	Sy1.9	0.0062	26.6	43.31	15A-Q-3	K	10 × 400	0.18	128
NGC 5899[a]	SAB(rs)c	Sy2	0.0086	36.9	42.53	13A-Q-48	K_l	10 × 450	0.13	178
NGC 6240[f]	I0: pec	Sy1.9	0.0245	105.0	43.97	07A-Q-62	K	16 × 300	0.19	509
Mrk3[g]	S0?	Sy1.9	0.0135	57.9	43.79	10A-Q-56	K_l	6 × 600	0.13	280
Mrk348	SA(s)0/a:	Sy 2	0.0150	64.3	43.86	11B-Q-71	K_l	6 × 400	0.18	311
Mrk607[a]	Sa? edge-on	Sy2	0.0089	38.1	42.36	12B-Q-45	K_l	12 × 500	0.14	184
Mrk1066[h]	$(R)SB0^+(s)$	Sy2	0.0120	51.4	42.51	08B-Q-30	K_l	8 × 600	0.15	249
ESO578-G009[i]†	Sc	Sy1.9	0.0350	150.0	43.59	17A-FT-10	K	6 × 600	0.35	727
CygnusA	S?	Sy2	0.0561	240.4	45.04	06A-C-11	K	7 × 900	0.18	1165
				type 1						
NGC 1275[j]	E pec	Sy1.5	0.0176	75.5	43.76	19A-Q-106	K	6 × 600	0.22	365
NGC 3227[a]	SAB(s)a pec	Sy1.5	0.0039	16.7	42.58	16A-Q-6	K	6 × 400	0.12	81
NGC 3516[a]	$(R)SB0^0?(s)$	Sy1.2	0.0088	37.7	43.29	15A-Q-3	K	10 × 450	0.15	182
NGC 4051[k]	SAB(rs)bc	Sy1.5	0.0023	9.9	41.69	06A-SV-123	K	6 × 750	0.18	47
NGC 4151[l]	(R')SAB(rs)ab?	Sy1.5	0.0033	14.1	43.17	06B-C-9	K	8 × 90	0.18	68
NGC 4235	SA(s)a edge-on	Sy1.2	0.0080	34.3	42.74	16A-Q-6	K	10 × 400	0.13	166
NGC 4395[m]	Sd	Sy1	0.0011	4.7	40.86	10A-Q-38	K	9 × 600	0.20	22
NGC 5548[n]	(R')SA0/a(s)	Sy1.5	0.0172	73.7	43.76	12A-Q-57	K_l	12 × 450	0.20	357
NGC 6814	SAB(rs)bc	Sy1.5	0.0052	22.3	42.59	13B-Q-5	K	113 × 120	0.18	108
Mrk79[o]	SBb	Sy1.5	0.0222	95.1	43.68	10A-Q-42	K_l	6 × 550	0.25	461
Mrk352[p]	SA0	Sy1.2	0.0149	63.8	43.19	12A-Q-42	K_l	11 × 400	0.37	309
Mrk509	?	Sy1.2	0.0344	147.4	44.44	13A-Q-40	K_l	6 × 450	0.14	714
Mrk618	SB(s)b pec	Sy1.2	0.0355	152.1	43.73	18B-Q-138	K	5 × 600	0.18	737
Mrk766[q]	(R')SB(s)a?	Sy1.5	0.0129	55.3	42.99	10A-Q-42	K_l	6 × 550	0.19	268
Mrk926	Sab	Sy1.5	0.0469	201.0	44.76	18B-Q-138	K	6 × 600	0.17	974
Mrk1044	S?	Sy1	0.0165	70.7	42.86	18B-Q-109	K_l	6 × 600	0.19	342
Mrk1048	RING pec	Sy1.5	0.0431	184.3	44.12	18B-Q-138	K	6 × 600	0.22	893
MCG + 08-11-011	SB?	Sy1.5	0.0205	87.9	44.13	19A-Q-106	K	6 × 470	0.20	425

type 1 and type 2 AGN in our sample most likely follow similar distributions in these two parameters. As type 1 and 2 AGN follow the same distributions in terms of X-ray luminosity and redshift, we compare these subsamples in terms of other physical properties in the following sections.

2.2 Observations, data reduction and measurements

The observations were carried out with the NIFS instrument (McGregor et al. 2003) on the Gemini North Telescope from 2006 to 2019. NIFS has a square field of view of 3.″0 × 3.″0, divided into 29 slices with an angular sampling of 0.″103 × 0.″042. At the distances of the galaxies of our sample, the NIFS field of view varies from 60 × 60 pc^2 to 3.5 × 3.5 kpc^2. Most of the observations (34/36) used adaptive optics (AO) by coupling NIFS with the ALTtitude conjugate Adaptive optics for the InfraRed system. Only NGC 1125 and ESO578-G009 were observed without AO. The resulting angular resolutions are shown in Table 1 and are in the range 0.″11–0.″44. Distinct observational strategies were used during the observations, which include the use of K or K_{long} gratings and spatial dithering, resulting in different spatial and spectral coverage among galaxies. The spectral resolving power of NIFS in the K band is $R \approx 5290$. Telluric standard stars were observed just before and/or after the observations of each galaxy.

The data reduction followed the standard procedures (e.g. Riffel et al. 2017) using the GEMINI IRAF package, including the trimming

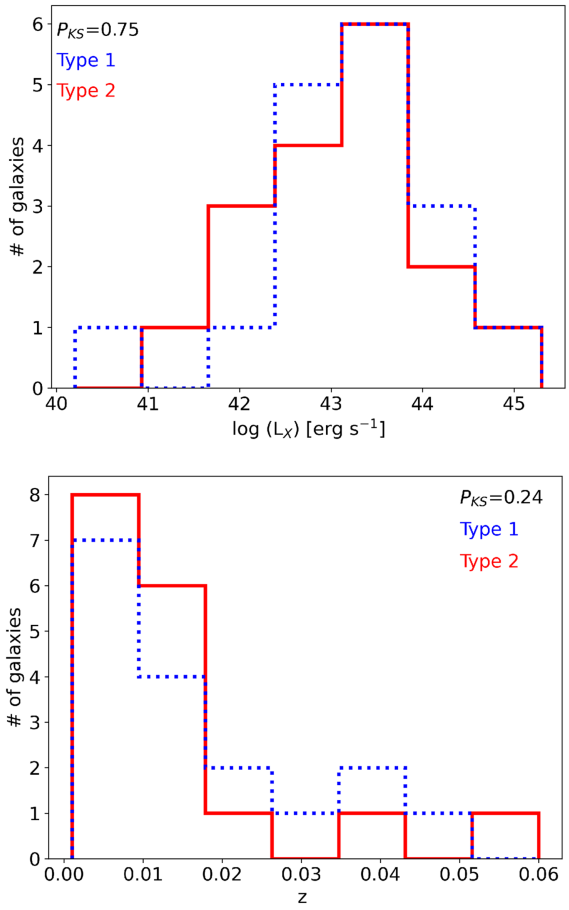

Figure 1. X-ray luminosity (top) and redshift (bottom) distributions of our sample, divided in type 1 (dashed-blue lines) and type 2 (continuous-red lines) AGN. In each panel, we show the probability of the null hypothesis ($P_{\rm KS}$) that type 1 and type 2 AGN follow similar distributions computed using the K–S test. The $P_{\rm KS}$ values indicate that type 1 and type 2 AGN of our sample do not follow distinct distributions in terms of L_X and z.

of the images, flat-fielding, cosmic ray rejection, sky subtraction, wavelength and s-distortion calibrations, removal of the telluric absorptions using the spectra of the telluric standard star and flux calibration by interpolating a blackbody function to the spectrum of the telluric standard. Finally, the data cubes were created at an angular sampling of 0.″05 × 0.″05 for each individual exposure and median combined using a sigma clipping algorithm to eliminate bad pixels and remaining cosmic rays and using the peak of the continuum emission of the galaxy as reference to perform the astrometry among the individual data cubes.

Results on gas emission properties of individual sources have already been published for 22 galaxies of our sample based on the *K*-band data used here. The references to these studies are shown in Table 1.

The *K*-band spectra of nearby active galaxies show plenty of H_2 emission lines and usually also present strong Brγ emission (e.g. Riffel et al. 2006). To obtain the emission-line flux distributions, we integrated the fluxes within a spectral window of 1500 km s^{-1} width centred at each emission line, after subtraction of the contribution of the underlying continuum fitted by a third order polynomial, similarly to the procedure adopted in Storchi-Bergmann et al. (2009). Our spectral window choice is very conservative, as the near-IR line widths in nearby galaxies are commonly much narrower than 1500 km s^{-1} and so our choice warrants that we are computing the total line fluxes. To minimize the effect of noise, we followed Liu et al. (2013) and first fitted each emission line by a combination of three Gaussian curves and the continuum by a linear equation using the IFSCUBE code (Ruschel-Dutra 2020). For type 1 AGN, we included an additional Gaussian to account for the broad Brγ component. Before computing the fluxes of Brγ in type 1 objects, we subtracted the contribution of this component and thus all measurements presented in this paper are for the narrow line components.

The fitting routine starts by modelling the spaxel corresponding to the peak of the continuum emission, using initial guesses for the centroid velocity and velocity dispersion of each component provided by the user. Then the IFSCUBE code performs the fitting of the neighbouring spaxles following a spiral loop and using the parameters from spaxels located at distances smaller than 0.″25 from the fitted spaxel as optimized guesses (as defined by the *refit* parameter). As mentioned above, we allow up to three Gaussian components to fit each line profile (four for the Brγ line in Sy 1), but the code finds the minimum number of Gaussians to reproduce the profiles by setting the initial guesses for the amplitudes of the unnecessary Gaussian functions to zero. The fit of multi Gaussians has no physical motivation, it merely aims at reproducing the observed profiles. The emission-line flux distributions measured directly from the observed data cubes are consistent with those obtained from the fits of the line profiles, but the direct measurements produce noisier maps, as already discussed in Liu et al. (2013).

3 RESULTS

3.1 Emission-line flux distributions and line-ratio maps

In Figs 2 and 3, we present examples of maps constructed from the Gemini NIFS data measurements, comprising: the continuum, H_2 2.1218 μm and Brγ flux distributions, the H_2 2.1218 μm/Brγ ratio map and Brγ equivalent width (*EqW*) map for selected type 2 and type 1 AGN, respectively. The maps for the other galaxies are shown in Figs A1 and A2 of the Appendix. We masked out regions where the amplitude of the line profile was smaller than three times the standard deviation of the continuum next to each line profile. The galaxies NGC 3393 (Sy 2) and Mrk 352 (Sy 1) do not present extended line emission and thus we do not show their corresponding maps. All other galaxies show extended emission in both H_2 and Brγ emission lines. The only exception is NGC 3516, for which the Brγ emission is seen only from the unresolved nucleus.

3.1.1 Flux distributions

The emission-line flux distributions present a wide variety of structures in both Brγ and H_2 emission. In most galaxies, the H_2 emission is more extended than the Brγ and the peak emission of both lines is observed at the galaxy nucleus. Other structures observed in the gas distribution comprise: nuclear spirals seen in molecular gas (e.g. Mrk 79); galaxies in which both H_2 and Brγ emission are seen mainly along the major axis of the large-scale disc (e.g. NGC 4235); galaxies in which the H_2 and Brγ emission are distributed along distinct orientations (e.g. NGC 4388); ring-like structures (e.g. Mrk 1044); galaxies with elongated H_2 emission and round Brγ flux distribution (e.g. Mrk 766), among other emission structures. There is no clear difference between the emission-line flux distributions of type 1 and type 2 AGN. A qualitative inspection of the H_2 and Brγ flux maps in

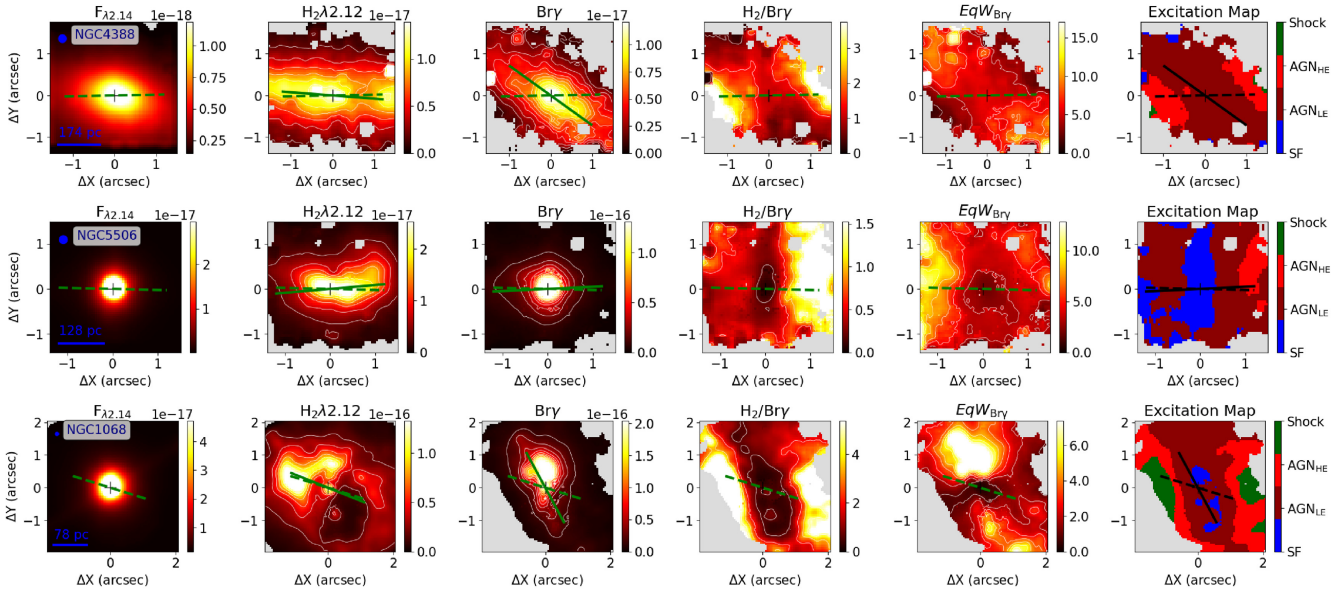

Figure 2. Selected maps for type 2 AGN. From left to right: *K*-band continuum obtained within a spectral window of 100 Å centred at 2.14 μm, H_2 2.1218 μm flux distribution, Brγ flux distribution, H_2/Brγ ratio map, Brγ equivalent width map, and excitation map. The colour bars show the continuum in units of erg s^{-1} cm^{-2} Å^{-1} spaxel^{-1}, the emission-line fluxes in erg s^{-1} cm^{-2} spaxel^{-1}, and the Brγ equivalent width in Å. The excitation map identifies with different colours the regions with typical H_2/Brγ values for: star forming regions (SF: H_2/Brγ < 0.4), low excitation AGN (AGN$_{LE}$: $0.4 \leq H_2/Br\gamma < 2$), and high excitation AGN (AGN$_{HE}$: $2 \leq H_2/Br\gamma < 6$) and shock-dominated objects (Shock: $H_2/Br\gamma > 6$). In each row, the name of the galaxy is identified in the continuum image, the filled circle corresponds to the angular resolution, the spatial scale is shown in the bottom-left corner of the continuum image, and the cross marks the position of the peak of the continuum emission. The dashed line indicates the orientation of the galaxy major axis obtained from the Hyperleda database. The continuous line on the flux maps shows the orientation of the emission-line flux distributions. The continuous line on the excitation map shows the orientation of the Brγ emission. The grey regions indicate locations where emission lines are not detected above three times the continuum noise amplitude (3σ). For all galaxies, north is up and east is to the left.

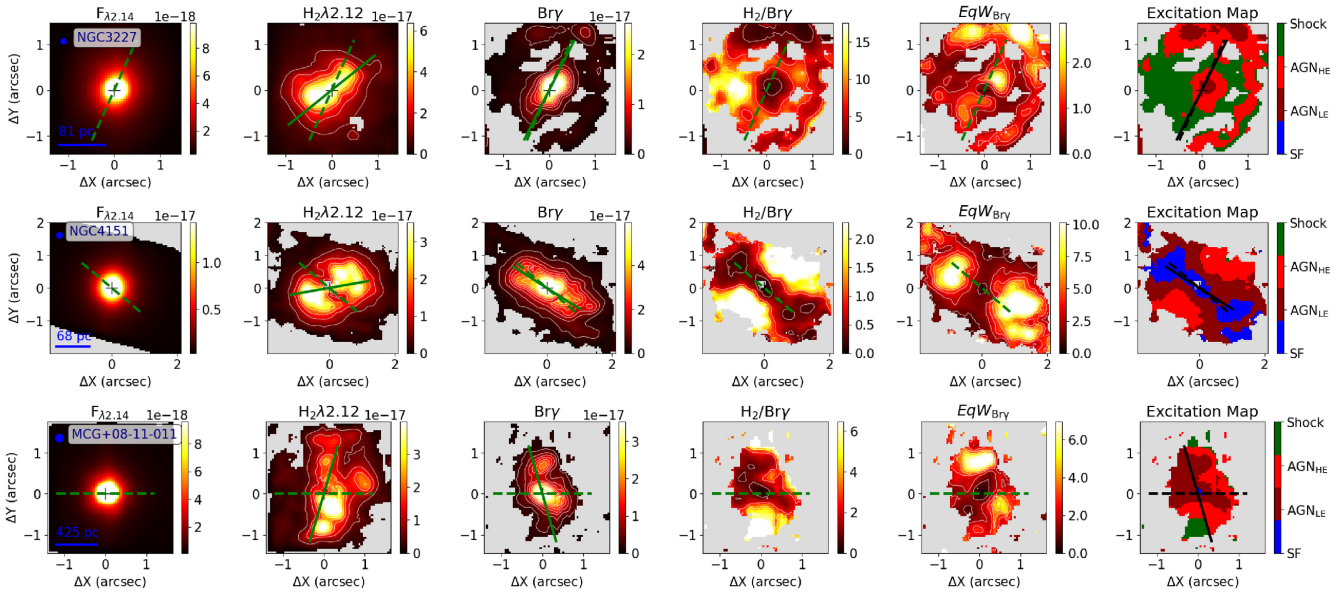

Figure 3. Examples of maps for type 1 AGN. Same as Fig. 2, but for type 1 AGN.

each object (Figs 2, 3, A1, and A2) shows that the Brγ usually traces a more collimated emission, while the H_2 emission spreads more over the whole field of view. This result is consistent with previous studies where the H_2 and ionized gas have been shown to present distinct flux distributions and kinematics (Riffel et al. 2018; Schönell et al. 2019).

We compute the radii that contain 50 per cent of the total flux (R_{50}) of H_2 2.1218 μm and Brγ emission lines. Although this parameter can be affected by projection effects if the H_2 and Brγ emission originate from distinct spatial locations in individual targets, the R_{50} is useful to compare the H_2 and Brγ emission in the whole sample. The corresponding R_{50} values for H_2 and Brγ are shown in Table 2

Table 2. (1) Galaxy name, (2) position angle of the large-scale disc from Hyperleda database, (3) H_2 and (4) and Brγ (4) position flux distribution position angles, (5) and (6) radii that contain half of the total flux of H_2 2.1218 μm and Brγ. All angles are measured east of north.

Galaxy	Ψ_0 (deg)	PA_{H_2} (deg)	$PA_{Br\gamma}$ (deg)	R_{50H_2} (pc)	$R_{50Br\gamma}$ (pc)
(1)	(2)	(3)	(4)	(5)	(6)
			type 2		
NGC 788	108.1	39.8 ± 1.6	89.4 ± 3.2	254 ± 42	296 ± 42
NGC 1052	112.7	44.0 ± 1.8	162.0 ± 7.7	62 ± 15	46 ± 15
NGC 1068	72.7	68.3 ± 1.2	28.3 ± 0.6	106 ± 11	71 ± 11
NGC 1125	53.5	46.5 ± 1.4	56.7 ± 1.2	137 ± 34	102 ± 34
NGC 1241	147.7	157.7 ± 4.6	46.9 ± 0.7	126 ± 42	126 ± 42
NGC 2110	175.1	143.4 ± 2.2	152.5 ± 0.9	145 ± 24	121 ± 24
NGC 4258	150.0	20.3 ± 2.6	13.2 ± 7.5	32 ± 4	28 ± 4
NGC 4388	91.1	85.6 ± 1.0	54.3 ± 0.8	183 ± 26	183 ± 26
NGC 5506	88.7	94.9 ± 1.3	92.8 ± 4.3	96 ± 19	57 ± 19
NGC 5899	20.8	10.3 ± 1.0	170.7 ± 1.7	80 ± 26	53 ± 26
NGC 6240	12.2	0.9 ± 0.7	178.5 ± 0.8	610 ± 76	458 ± 768
Mrk3	15.0	73.7 ± 1.3	80.9 ± 1.2	210 ± 42	168 ± 42
Mrk348	87.0	160.8 ± 2.2	7.5 ± 5.9	186 ± 46	93 ± 46
Mrk607	137.3	134.8 ± 1.2	140.6 ± 2.2	110 ± 27	55 ± 27
Mrk1066	112.3	118.8 ± 1.5	126.0 ± 0.3	224 ± 37	186 ± 37
ESO578-G009	27.6	29.9 ± 0.6	29.3 ± 0.7	1199 ± 109	654 ± 109
CygnusA	151.0	176.1 ± 1.8	140.6 ± 1.0	1049 ± 174	1049 ± 174
			type 1		
NGC 1275	110.0	42.2 ± 6.1	137.9 ± 2.2	164 ± 54	109 ± 54
NGC 3227	156.0	128.8 ± 3.1	153.1 ± 2.2	60 ± 12	36 ± 12
NGC 3516	55.0	138.0 ± 4.0	–	± 27	27 ± 27
NGC 4051	139.4	96.9 ± 1.5	117.4 ± 4.6	35 ± 7	14 ± 7
NGC 4151	50.0	100.0 ± 1.0	57.5 ± 0.4	61 ± 10	51 ± 10
NGC 4235	49.0	43.4 ± 0.5	42.6 ± 0.6	224 ± 24	249 ± 24
NGC 4395	127.8	106.4 ± 3.2	104.3 ± 5.2	10 ± 4	10 ± 4
NGC 5548	118.2	146.0 ± 3.8	46.2 ± 2.3	160 ± 53	160 ± 53
NGC 6814	107.6	121.2 ± 1.3	153.2 ± 1.3	48 ± 16	48 ± 16
Mrk79	73.0	176.2 ± 3.9	171.9 ± 35.1	276 ± 69	207 ± 69
Mrk509	80.0	139.4 ± 5.1	96.3 ± 4.3	536 ± 107	428 ± 107
Mrk618	85.0	39.4 ± 2.2	24.8 ± 3.9	442 ± 110	221 ± 110
Mrk766	73.1	62.0 ± 1.4	135.1 ± 1.1	160 ± 40	120 ± 40
Mrk926	104.1	71.7 ± 4.2	104.0 ± 2.9	730 ± 146	438 ± 146
Mrk1044	177.5	169.2 ± 2.2	6.5 ± 7.9	359 ± 51	102 ± 51
Mrk1048	80.3	135.4 ± 1.5	167.4 ± 3.0	536 ± 134	536 ± 134
MCG + 08-11-01	90.0	163.6 ± 1.3	16.0 ± 2.4	383 ± 63	191 ± 63

and Fig. 4 shows the comparison between R_{50H2} and $R_{50Br\gamma}$. The Brγ flux distribution is more concentrated than that of H_2 and the R_{50} for the H_2 is on average 56 per cent larger than that of Brγ.

We use the CV2.MOMENTS python package to compute the moments and orientation of the H_2 and Brγ flux distributions. The orientations are shown as the continuous lines in the flux maps of Figs 2, 3, A1, and A2. The position angles (PAs) are listed in Table 2, together with the orientation of the major axis of the galaxy obtained from the Hyperleda database (Paturel et al. 2003), measured from the 25 mag arcsec^2 isophote in a B-band image. We performed Monte Carlo simulations with 100 iterations each to compute the uncertainties, by adding random noise with amplitude of the 20th percentile flux value of the corresponding map. The listed uncertainties in Table 2 correspond to the standard deviation of the mean of the simulations.

We have compared the PA offset (ΔPA) between the major axis of the large-scale disc and the orientation of the Brγ and H_2 flux distributions. Although the orientations of both flux distributions vary, the K–S test ($P_{KS} = 0.97$) indicates the distributions of the corresponding ΔPA for Brγ and H_2 are not distinct. $\Delta PA > 30^\circ$ is usually used as a threshold to determine whether the stellar and gas discs are misaligned (Jin et al. 2016). We find ΔPA larger than this value in 15 galaxies (42 per cent) for the Brγ and in 16 galaxies (44 per cent) for H_2. These fractions are higher than those between the kinematic PA of the stellar velocity field in the inner 3 × 3 arcsec^2 and the major axis of the large-scale disc, of ∼18 per cent (Riffel et al. 2017), suggesting an origin in non-circular motions in the gas. The distributions of the ΔPA between the orientation of the H_2 and Brγ flux distributions (PA_{H2}-$PA_{Br\gamma}$) for type 1 and type 2 AGN are similar. We find $\Delta PA > 30^\circ$ for 15 galaxies (45 per cent). Three galaxies (NGC 1275, NGC 5548, and Mrk 766) of these show $\Delta PA > 60^\circ$, for which the H_2 emission is observed mainly along the major axis of the galaxy.

3.1.2 *Line ratios*

The H_2 2.1218 μm/Brγ emission-line ratio is commonly used to investigate the main source of the H_2 excitation (Reunanen,

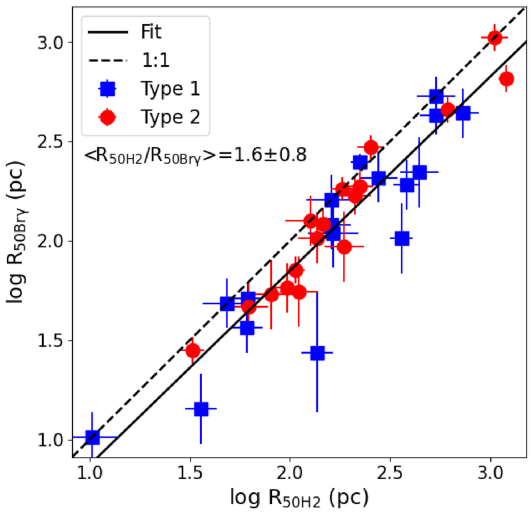

Figure 4. Comparison of the radii that contain 50 per cent of the total flux of $H_2$2.1218 μm and Brγ. The dashed line shows the 1:1 relation and the continuous line shows the best fit of the data by a first order polynomial, given by $\log R_{50\,\mathrm{Br}\gamma} = (0.98 \pm 0.20) \times \log R_{50\,\mathrm{H_2}} - (0.10 \pm 0.44)$.

Kotilainen & Prieto 2002; Rodríguez-Ardila et al. 2004, 2005; Storchi-Bergmann et al. 2009; Riffel, Storchi-Bergmann & Nagar 2010a; Riffel et al. 2013a, 2014; Schönell et al. 2014, 2019; Colina et al. 2015; Dahmer-Hahn et al. 2019b; Fazeli et al. 2020; Riffel 2020). Small values ($H_2/\mathrm{Br}\gamma \lesssim 0.4$) are usually observed in H II regions and star forming galaxies, while AGN present $0.4 \lesssim H_2/\mathrm{Br}\gamma \lesssim 6.0$ and higher values are usually observed in LINERs and shock-dominated regions (e.g. Riffel et al. 2013a, 2021; Colina et al. 2015). In the near-IR, the line ratio limits are empirical and their excitation mechanisms are less understood than those of the optical lines (e.g. Rodríguez-Ardila et al. 2004, 2005). However, it is worth mentioning that the $H_2/\mathrm{Br}\gamma$ line ratio can be affected by the geometry of the H II region (Puxley, Hawarden & Mountain 1990) and the velocity of the shock (Wilgenbus et al. 2000). Both properties affect the dissociation of the H_2 molecule, making the fraction of H_2, and the $H_2/\mathrm{Br}\gamma$ ratio, to change. The $H_2/\mathrm{Br}\gamma$ maps for our sample (Figs 2, 3, A1, and A2) show values ranging from nearly zero, as seen in the rings of star forming regions of Mrk 1044 and for NGC 4151 – in which the H_2 emission decreases due to the dissociation of the molecule by the strong AGN radiation field (e.g. Storchi-Bergmann et al. 2009) – to values of up to $H_2/\mathrm{Br}\gamma \sim 30$ for NGC 1275, where the H_2 emission originates in shocks produced by AGN winds (Riffel et al. 2020).

We build excitation maps (fifth column of Figs 2, 3, A1, and A2) to spatially locate the regions where different excitation mechanisms may be occurring. All galaxies present spaxels dominated by AGN excitation ($0.4 < H_2/\mathrm{Br}\gamma < 6$), and in order to map the variation of this excitation, we have divided the AGN regions into low ($0.4 \leq H_2/\mathrm{Br}\gamma < 2$) and high excitation ($2 \leq H_2/\mathrm{Br}\gamma < 6$). This separation allows us to further investigate the origin of the H_2 emission in the AGN. A similar separation was done in Riffel et al. (2020) to split the high line ratio region in the H_2 2.1218 μm/Brγ versus [Fe II]1.2570 μm/Paβ diagnostic diagram.

Table 3 presents the median $H_2/\mathrm{Br}\gamma$ ratio over the whole FoV ($H_2/\mathrm{Br}\gamma_{\mathrm{MED}}$) for each galaxy of our sample, the median value within $r < 125$ pc ($H_2/\mathrm{Br}\gamma_{r<125\mathrm{pc}}$), the nuclear ratio, computed using an aperture with radius equal to the angular resolution of the data for each galaxy ($H_2/\mathrm{Br}\gamma_{\mathrm{nuc}}$), and the extra-nuclear line ratio, measured as the median value of spaxels located at distances from the galaxy nucleus larger than the angular resolution ($H_2/\mathrm{Br}\gamma_{\mathrm{extra}}$). The median values of $H_2/\mathrm{Br}\gamma$ are within the AGN range for 31 (91 per cent) galaxies of our sample. The exceptions are NGC 6240, NGC 1275, and Mrk 3 that show $H_2/\mathrm{Br}\gamma$ median values of 11.76, 11.10, and 0.17, respectively. The high $H_2/\mathrm{Br}\gamma_{\mathrm{MED}}$ values are consistent with shocks as the dominant H_2 excitation mechanism (Ilha et al. 2016; Müller-Sánchez et al. 2018a; Riffel et al. 2020). The low ratios observed for Mrk 3, NGC 5506, and NGC 4151 may be explained by the dissociation of the H_2 molecule by the AGN radiation field in these galaxies as proposed by previous works (Storchi-Bergmann et al. 2009; Gnilka et al. 2020). As seen in Table 3, type 1 and type 2 AGN show similar values of $H_2/\mathrm{Br}\gamma$ median values.

Table 3. $H_2/\mathrm{Br}\gamma$ line ratio: (1) galaxy name, (2) median values of the line ratio for the whole FoV ($H_2/\mathrm{Br}\gamma_{\mathrm{MED}}$), (3) in the inner $r <$ 125 pc ($H_2/\mathrm{Br}\gamma_{r<125\mathrm{pc}}$), (4) wihin the central angular resolution element ($H_2/\mathrm{Br}\gamma_{\mathrm{nuc}}$), and (5) for spaxels at distances larger than the angular resolution radius ($H_2/\mathrm{Br}\gamma_{\mathrm{extra}}$).

Galaxy (1)	$H_2/\mathrm{Br}\gamma_{\mathrm{MED}}$ (2)	$H_2/\mathrm{Br}\gamma_{r<125\mathrm{pc}}$ (3)	$H_2/\mathrm{Br}\gamma_{\mathrm{nuc}}$ (4)	$H_2/\mathrm{Br}\gamma_{\mathrm{extra}}$ (5)
		type 2		
NGC 788	0.96 ± 0.91	0.82 ± 0.35	0.53 ± 0.05	0.96 ± 0.91
NGC 1052	2.32 ± 1.07	2.32 ± 1.07	2.15 ± 0.27	2.36 ± 1.09
NGC 1068	1.78 ± 3.18	1.30 ± 3.72	0.54 ± 0.10	1.79 ± 3.18
NGC 1125	0.78 ± 0.62	0.39 ± 0.06	0.38 ± 0.04	0.88 ± 0.62
NGC 1241	3.11 ± 2.21	3.21 ± 1.58	2.67 ± 0.09	3.18 ± 2.24
NGC 2110	3.61 ± 1.57	3.15 ± 1.57	1.36 ± 0.38	3.65 ± 1.55
NGC 4258	1.84 ± 0.90	1.84 ± 0.90	2.59 ± 1.47	1.81 ± 0.85
NGC 4388	1.25 ± 1.16	1.31 ± 0.38	1.15 ± 0.16	1.26 ± 1.17
NGC 5506	0.51 ± 0.68	0.43 ± 0.45	0.09 ± 0.02	0.51 ± 0.68
NGC 5899	4.35 ± 4.13	4.27 ± 4.38	2.40 ± 0.13	4.41 ± 4.15
NGC 6240	11.78 ± 7.49	8.55 ± 4.70	8.65 ± 3.96	11.95 ± 7.86
Mrk3	0.17 ± 0.15	0.07 ± 0.04	0.04 ± 0.01	0.18 ± 0.15
Mrk348	1.30 ± 0.84	0.89 ± 0.28	0.56 ± 0.09	1.34 ± 0.83
Mrk607	1.06 ± 0.69	0.93 ± 0.37	0.51 ± 0.06	1.08 ± 0.69
Mrk1066	1.39 ± 1.51	1.41 ± 0.55	1.41 ± 0.16	1.39 ± 1.51
ESO578-G009	1.60 ± 1.77	2.97 ± 0.77	2.17 ± 1.17	1.59 ± 1.79
CygnusA	2.06 ± 1.75	1.92 ± 0.14	1.93 ± 0.27	2.08 ± 1.76
Mean	2.35 ± 2.58	2.10 ± 1.96	1.71 ± 1.94	2.38 ± 2.62
		type 1		
NGC 1275	11.09 ± 5.27	12.40 ± 3.95	7.56 ± 2.33	11.42 ± 5.37
NGC 3227	5.72 ± 3.84	5.89 ± 3.81	1.84 ± 0.41	5.75 ± 3.83
NGC 3516	2.31 ± 0.86	2.47 ± 0.74	2.14 ± 0.42	2.61 ± 0.99
NGC 4051	3.16 ± 2.03	3.16 ± 2.03	0.53 ± 0.08	3.19 ± 2.02
NGC 4151	0.76 ± 1.16	0.79 ± 1.19	0.21 ± 0.07	0.78 ± 1.16
NGC 4235	3.71 ± 1.88	3.10 ± 1.29	–	3.71 ± 1.88
NGC 4395	1.01 ± 0.88	1.01 ± 0.88	0.79 ± 0.06	1.02 ± 0.89
NGC 5548	1.37 ± 0.48	1.27 ± 0.33	1.17 ± 0.14	1.39 ± 0.49
NGC 6814	5.55 ± 6.00	5.73 ± 41.48	18.57 ± 149.12	5.34 ± 6.45
Mrk79	2.83 ± 1.61	2.59 ± 0.79	2.56 ± 0.74	2.87 ± 1.66
Mrk509	0.91 ± 0.64	0.41 ± 0.60	0.23 ± 0.19	0.91 ± 0.63
Mrk618	1.24 ± 1.97	0.44 ± 0.04	0.44 ± 0.04	1.28 ± 1.99
Mrk766	0.80 ± 1.02	0.34 ± 0.12	0.13 ± 0.04	0.82 ± 1.03
Mrk926	1.83 ± 0.80	1.71 ± 0.19	1.72 ± 0.28	1.85 ± 0.82
Mrk1044	0.68 ± 0.52	0.05 ± 0.01	–	0.68 ± 0.52
Mrk1048	1.75 ± 1.42	3.25 ± 1.12	3.07 ± 1.90	1.69 ± 1.32
MCG + 08-11-01	2.19 ± 2.65	1.01 ± 0.77	0.70 ± 0.41	2.31 ± 2.66
Mean	2.76 ± 2.57	2.68 ± 2.96	2.78 ± 4.59	2.80 ± 2.62

We use K–S statistics to test whether the distributions of $H_2/\mathrm{Br}\gamma_{\mathrm{MED}}$ for type 1 and type 2 AGN are distinct. We find $P_{\mathrm{KS}} = 0.96$, meaning that likely the $H_2/\mathrm{Br}\gamma_{\mathrm{MED}}$ distributions of type 1 and type 2 AGN are drawn from the same underlying distribution. However, our observations cover spatial scales from a few tens of pc to a few kpc, and so, for the most distant objects the $H_2/\mathrm{Br}\gamma_{\mathrm{MED}}$ is dominated by the extra-nuclear regions, while in the closest galaxies, the contribution of the nuclear emission is higher. In order to avoid this problem, we compute the $H_2/\mathrm{Br}\gamma$ within the inner 125 pc radius for all objects. This aperture corresponds to the lowest spatial resolution in our sample (for ESO578-G009). For three galaxies

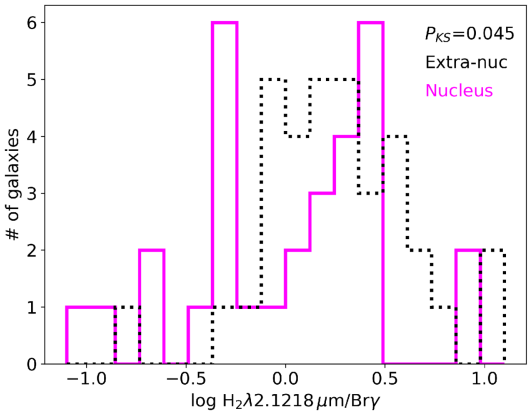

Figure 5. Nuclear (magenta) and extra-nuclear (dotted black) $H_2/Br\gamma$ distributions of the galaxies of our sample.

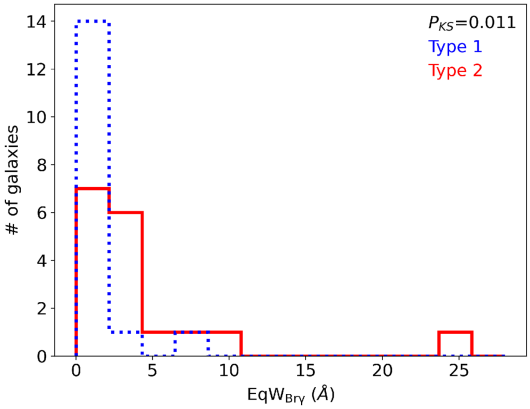

Figure 6. Nuclear Brγ equivalent width distributions for the type 1 (dashed-blue lines) and type 2 (continuous-red lines) AGN in our sample. The equivalent widths are measured within apertures corresponding to the angular resolution of the data.

(NGC 4258, NGC 4051, and NGC 4395), the FoV is smaller than 125 pc radius and thus, we use the whole FoV to compute the $H_2/Br\gamma$ in these cases. The K–S test indicates again that type 1 and type 2 AGN do not have distinct distributions of $H_2/Br\gamma$ within the inner 125 pc radius. Similarly, we do not find a statistically significant difference in the nuclear $H_2/Br\gamma$ distributions (computed for an aperture corresponding to the angular resolution of the data for each galaxy) for type 1 and type 2 AGN. Finally, we test whether $H_2/Br\gamma$ (median, within 125 pc radius and nuclear) and the hard X-ray luminosity are correlated using the Pearson test, resulting that these parameters do not present a statistically significant correlation.

Fig. 5 shows the only distinct distributions we found: the $H_2/Br\gamma_{nuc}$ and $H_2/Br\gamma_{extra}$ ones. Using the K–S test, we obtain $P_{KS} = 0.045$ indicating that the distributions are distinct: on average, the nucleus presents lower $H_2/Br\gamma$ ratios than the extra-nuclear regions.

3.2 Brγ equivalent width maps

The fifth column of Figs 2, 3, A1, and A2 shows the Brγ equivalent width ($EqW_{Br\gamma}$) maps. The emission structures are better seen in the $EqW_{Br\gamma}$ than in the flux distribution maps, as the former measure the emission relative to the continuum. For example, in Mrk 3 (Fig. A1), the $EqW_{Br\gamma}$ map shows knots of emission not easily observed in the Brγ flux map. Young (<10 Myr) stellar populations present $EqW_{Br\gamma} \gtrsim 50$ Å, as predicted by evolutionary photoionization models (Dors et al. 2008; Riffel et al. 2009a). All galaxies of our sample clearly show smaller values ($EqW_{Br\gamma} \lesssim 30$ Å) than those predicted for young stellar population models. Even galaxies with known active star formation, as NGC 6240 (e.g. Keel 1990; Lutz et al. 2003; Pasquali, Gallagher & de Grijs 2004) and NGC 3227 (Gonzalez Delgado & Perez 1997; Schinnerer, Eckart & Tacconi 2000), present low $EqW_{Br\gamma}$ values, which suggest the near-IR continuum is dominated by the contribution of old stellar populations and the AGN featureless continuum in the nucleus.

Differently from the Brγ flux distributions, which usually present the emission peak at the nucleus, the highest values of $EqW_{Br\gamma}$ are seen away from the nucleus in most galaxies of our sample. In addition, a visual inspection of the $EqW_{Br\gamma}$ maps shows a drop in the $EqW_{Br\gamma}$ values at the nucleus. This drop is more prominent in type 1 AGN than in type 2, possibly due to a stronger dilution of the Brγ emission by the nuclear continuum.

We measure the $EqW_{Br\gamma}$ values for the nucleus of each galaxy within an aperture corresponding to the angular resolution of the data and compare the $EqW_{Br\gamma}$ distributions of type 1 and type 2 AGN and find that they follow distinct distributions ($P_{KS} = 0.011$). Fig. 6 shows the $EqW_{Br\gamma}$ distributions for type 1 AGN (in blue) and type 2 (in red) AGN. A slightly higher P_{KS} (0.045) is obtained by comparing the Brγ equivalent widths within the same spatial region of all galaxies (125 pc radius) implying the null hypothesis in which type 1 and type 2 AGN follow the same underlying distribution is rejected at the 95 per cent confidence level. On the other hand, the comparison of the median $EqW_{Br\gamma}$ distributions over the whole FoV results in $P_{KS} = 0.465$, meaning that the null hypothesis cannot be rejected and likely type 1 and type 2 AGN originate from the same underlying $EqW_{Br\gamma}$ distribution. The Pearson test shows that $EqW_{Br\gamma}$ does not correlate with L_X. This result suggests that there is no intrinsic difference between these type 1 and type 2 AGN, just circumstantial due orientation so that, at larger scales, where the central source is not seen, no clear distinction can be made between the two.

3.3 Masses of hot molecular and ionized hydrogen

We use the fluxes of the H_2 2.12 μm and Brγ emission lines to compute the mass of hot molecular (M_{H_2}) and ionized ($M_{H\,II}$) hydrogen. The mass of hot molecular gas (M_{H_2}) can be estimated, under the assumptions of local thermal equilibrium and excitation temperature of 2000 K, by (e.g. Scoville et al. 1982; Riffel et al. 2014):

$$\left(\frac{M_{H_2}}{M_\odot}\right) = 5.0776 \times 10^{13} \left(\frac{F_{H_2\,2.1218}}{\mathrm{erg\,s^{-1}\,cm^{-2}}}\right) \left(\frac{D}{\mathrm{Mpc}}\right)^2, \quad (1)$$

where $F_{H_2\,2.1218}$ is the H_2 2.1218μm emission-line flux and D is the distance to the galaxy.

Following Osterbrock & Ferland (2006) and Storchi-Bergmann et al. (2009), we estimate the mass of ionized gas $M_{H\,II}$ by

$$\left(\frac{M_{H\,II}}{M_\odot}\right) = 3 \times 10^{19} \left(\frac{F_{Br\gamma}}{\mathrm{erg\,cm^{-2}\,s^{-1}}}\right) \left(\frac{D}{\mathrm{Mpc}}\right)^2 \left(\frac{N_e}{\mathrm{cm^{-3}}}\right)^{-1}, \quad (2)$$

where $F_{Br\gamma}$ is the Brγ flux (summing the fluxes of all spaxels) and N_e is the electron density. Recent studies find that the electron densities in ionized outflows are underestimated using the [S II] line ratio (Baron & Netzer 2019; Davies et al. 2020). However, most of the Brγ emission in the inner kpc of nearby Seyfert galaxies originate from gas rotating in the plane of the disc (e.g. Riffel et al. 2018; Schönell et al. 2019), and thus we adopt $N_e = 500\,\mathrm{cm^{-3}}$, which is a typical value measured in AGN from the [S II]λλ6717,6730 lines

Table 4. Ionized and hot H_2 gas masses and H_2 excitation temperatures. (1) Name of the galaxy; (2 & 3) Hot Molecular and ionized hydrogen masses within the inner 125 pc radius and (4 & 5) in the whole field of view; (6 & 7) H_2 vibrational and rotational temperatures.

Galaxy	$M_{H_2\, r<125pc}$ (10^1 $M_\odot$)	$M_{H\,II\, r<125pc}$ (10^4 $M_\odot$)	$M_{H_2\,FoV}$ (10^1 $M_\odot$)	$M_{H\,II\,FoV}$ (10^4 $M_\odot$)	T_{vib} (K)	T_{rot} (K)
(1)	(2)	(3)	(4)	(5)	(6)	(7)
			type 2			
NGC 788	12.8 ± 0.5	19.5 ± 0.6	59.0 ± 5.6	83.4 ± 9.2	2149 ± 80	810 ± 567
NGC 1052	11.0 ± 1.1	5.7 ± 1.6	11.9 ± 1.4	5.8 ± 1.8	4233 ± 306	–
NGC 1068	202.5 ± 2.2	193.1 ± 3.8	288.6 ± 4.2	222.2 ± 6.2	2474 ± 11	1551 ± 332
NGC 1125	21.3 ± 0.7	64.1 ± 0.8	41.7 ± 3.9	94.1 ± 6.4	3857 ± 161	1345 ± 633
NGC 1241	34.9 ± 0.7	13.0 ± 0.9	51.0 ± 5.4	19.4 ± 4.3	3746 ± 123	832 ± 753
NGC 2110	41.7 ± 0.8	16.8 ± 1.0	100.5 ± 3.1	27.4 ± 2.1	2512 ± 23	–
NGC 4258	–	–	0.7 ± 0.1	0.3 ± 0.1	5132 ± 2490	–
NGC 4388	40.0 ± 1.1	35.3 ± 1.5	119.6 ± 5.8	101.5 ± 6.4	2725 ± 33	1065 ± 593
NGC 5506	45.7 ± 0.7	174.1 ± 1.4	66.8 ± 2.0	204.8 ± 4.3	2746 ± 24	1154 ± 358
NGC 5899	17.8 ± 0.8	6.6 ± 1.1	21.4 ± 2.4	7.1 ± 3.5	2853 ± 76	–
NGC 6240	533.0 ± 1.6	99.0 ± 2.5	10926.4 ± 88.5	992.5 ± 34.2	2339 ± 3	1247 ± 74
Mrk3	23.6 ± 2.7	498.09.5 ± 4.9	99.6 ± 8.9	1167.2 ± 28.3	4953 ± 139	–
Mrk348	17.6 ± 0.6	27.3 ± 0.9	42.6 ± 6.1	39.4 ± 4.7	2932 ± 73	–
Mrk607	7.1 ± 0.4	11.3 ± 0.7	12.0 ± 1.2	13.1 ± 1.5	4079 ± 301	–
Mrk1066	57.4 ± 0.4	68.6 ± 0.7	228.4 ± 5.7	270.0 ± 8.7	2614 ± 19	–
ESO578-G009	0.4 ± 0.3	1.2 ± 1.3	251.6 ± 37.5	83.0 ± 19.3	4223 ± 298	757 ± 654
CygnusA	51.7 ± 0.3	32.5 ± 0.3	2163.2 ± 63.4	1109.3 ± 59.2	2777 ± 32	1352 ± 410
Mean	67.0 ± 121.1	74.5 ± 120.3	852.2 ± 2494.1	261.7 ± 393.1	3409 ± 955	1096 ± 302
			type 1			
NGC 1275	1170.3 ± 5.3	150.6 ± 8.5	2327.5 ± 56.7	229.8 ± 20.5	2309 ± 12	1021 ± 351
NGC 3227	52.1 ± 1.3	11.5 ± 1.2	53.7 ± 1.5	11.8 ± 1.3	2906 ± 27	1909 ± 586
NGC 3516	8.7 ± 2.2	2.0 ± 0.3	16.2 ± 2.7	2.1 ± 1.9	3583 ± 374	–
NGC 4051	–	–	7.4 ± 0.3	4.7 ± 0.6	3596 ± 88	1354 ± 876
NGC 4151	36.9 ± 1.3	54.7 ± 1.6	37.8 ± 1.8	56.8 ± 2.3	2495 ± 45	1365 ± 778
NGC 4235	4.0 ± 0.5	0.2 ± 0.1	13.7 ± 1.2	1.9 ± 0.5	5055 ± 1425	–
NGC 4395	–	–	0.2 ± 0.1	0.2 ± 0.1	2866 ± 70	2075 ± 656
NGC 5548	33.3 ± 5.5	32.1 ± 6.8	79.7 ± 28.5	71.2 ± 32.8	–	–
NGC 6814	7.8 ± 0.8	1.4 ± 0.4	8.6 ± 1.4	1.4 ± 0.6	3093 ± 115	1811 ± 812
Mrk79	52.9 ± 2.1	23.9 ± 2.5	195.6 ± 12.1	61.4 ± 6.7	3392 ± 95	–
Mrk509	8.2 ± 10.1	21.0 ± 9.3	213.8 ± 26.0	226.9 ± 22.3	3539 ± 320	–
Mrk618	62.5 ± 8.3	162.8 ± 10.4	507.1 ± 58.0	538.0 ± 82.7	4009 ± 291	752 ± 703
Mrk766	23.3 ± 2.0	112.2 ± 3.7	60.5 ± 7.3	166.5 ± 17.7	3278 ± 164	–
Mrk926	79.3 ± 12.5	54.7 ± 15.2	1340.8 ± 106.5	507.2 ± 53.0	3388 ± 173	1498 ± 932
Mrk1044	0.1 ± 0.1	53.5 ± 4.9	11.5 ± 3.1	81.7 ± 14.1	–	–
Mrk1048	23.4 ± 5.8	10.3 ± 8.2	620.6 ± 71.7	313.0 ± 67.3	3022 ± 145	875 ± 517
MCG + 08-11-01	117.6 ± 18.5	138.2 ± 19.7	1080.3 ± 56.8	424.8 ± 44.4	2560 ± 44	1212 ± 675
Mean	99.3 ± 269.6	49.0 ± 54.8	386.8 ± 622.2	158.8 ± 179.5	3298 ± 791	1254 ± 570

(e.g. Dors et al. 2014, 2020; Brum et al. 2017; Freitas et al. 2018; Kakkad et al. 2018). The distances to the galaxies adopted here are based on the galaxy redshift (Table 1) for all targets.

Table 4 shows the mass of hot H_2 and ionized hydrogen for the galaxies of our sample computed in the whole NIFS FoV (M_{H_2FoV} and $M_{H\,IIFoV}$) and within the inner 125 pc ($M_{H_2\,r<125pc}$ and $M_{H\,II\,r<125pc}$). The corresponding distributions are shown in Fig. 7. For three galaxies (NGC 4258, NGC 4041, and NGC 4395), the FoV is smaller than 250 pc and so, we do not calculate the mass within the inner 125 pc radius. We do not find statistically significant differences between the masses of ionized and molecular gas of type 1 and type 2 AGN.

3.4 H_2 vibrational and rotational temperatures

The H_2 1–0 S(1) 2.1218 μm/2-1 S(1) 2.2477 μm and 1–0 S(2) 2.0338 μm/1–0 S(0) 2.2235 μm line ratios can be used to estimate the vibrational and rotational temperatures of H_2. Using $N_i/g_i = F_i\lambda_i/(A_i g_i) = \exp[-E_i/(k_B T_{exc})]$, where N_i are the column densities in the upper level, g_i the statistical weights, F_i and λ_i are the line fluxes and wavelengths, A_i are the transition probabilities, E_i are the energies of the upper level, T_{exc} is the excitation temperature, and k_B is the Boltzmann constant. Using the transition probabilities from Turner, Kirby-Docken & Dalgarno (1977), the rotational temperature is given by:

$$T_{rot} \cong -\frac{1113}{\ln\left(0.323\frac{F_{H_2\,2.0338}}{F_{H_2\,2.2235}}\right)} \quad (3)$$

and the vibrational temperature by

$$T_{vib} \cong \frac{5594}{\ln\left(1.355\frac{F_{H_2\,2.1218}}{F_{H_2\,2.2477}}\right)}. \quad (4)$$

We were able to estimate the H_2 vibrational temperature for 32 galaxies. For NGC 5548 and Mrk 1044 at least one of the H_2 emission lines used to determine T_{vib} is not detected in our NIFS data with an amplitude larger than twice the standard deviation of the adjacent continuum. We estimate the H_2 rotational temperature

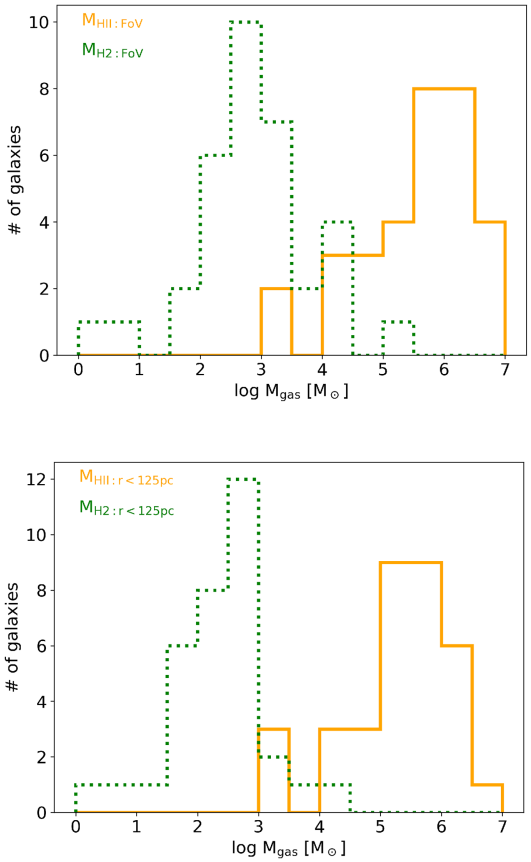

Figure 7. Molecular (green) and ionized (orange) hydrogen mass distributions for the galaxies of our sample, computed using the whole FoV (top) and the inner 125 pc radius (bottom).

for 21 galaxies. 11 galaxies of our sample were observed using the K_{long} grating (Table 1), for which the spectral range does not include the H_2 2.0338 μm emission line, needed to estimate the H_2 rotational temperature. In addition, this line is not detected for NGC 3516 and NGC 4235. In Figs A3 and A4, we show the maps of T_{rot} and T_{vib} for the type 2 and type 1 AGN and in Fig. A5, we show the T_{vib} maps for the objects where the spectral range does not include the 1–0 S(2) line. Table 4 shows the median temperatures for each galaxy. The median values of the vibrational temperature are in the range from ∼2100 to ∼4300 K, while the rotational temperatures are in the range ∼450–1900 K. There is no difference between the mean temperatures in type 1 and type 2 AGN.

4 DISCUSSION

4.1 Type 1 versus type 2 AGN

According to the AGN Unification Model (Antonucci 1993; Urry & Padovani 1995), type 1 and type 2 AGN represent the same class of objects seen at distinct viewing angles. However, some recent results suggest these two classes may be intrinsically distinct objects (e.g. Elitzur 2012; Elitzur, Ho & Trump 2014; Prieto et al. 2014; Villarroel & Korn 2014; Audibert et al. 2017), the tori of type 2 AGN having on average smaller opening angles and more clouds along the line of sight than for type 1 (Ramos Almeida et al. 2011).

Our sample presents the same number of type 1 and type 2 AGN and they follow similar luminosity and redshift distributions (Fig. 1), thus we can compare both AGN types in terms of the emission-line properties. We find the type 1 and type 2 AGN of our sample present similar H_2/Brγ line ratios, ionized and hot molecular gas masses and H_2 excitation temperature distributions. They also present no difference in terms of the ΔPA between the Brγ and H_2 flux distributions and between the orientation of the major axis of the hosts and the emission-line flux distributions. These results support the unification scenario.

We find a statistically significant difference between type 1 and type 2 AGN only for the emission line equivalent widths at the nucleus (Fig. 6). Seyfert 1 nuclei show smaller equivalent widths than Seyfert 2 nuclei. The *K*-band continuum of AGN can present a strong contribution of hot dust emission from the inner border of the torus (e.g. Riffel, Storchi-Bergmann & McGregor 2009c; Dumont et al. 2020). This component is present in about 90 per cent of Seyfert 1 nuclei, while only about 25 per cent of Seyfert 2 nuclei present this component (Riffel et al. 2009b). Thus, the smaller values of equivalent widths we observe in type 1 AGN may be due to stronger contributions of hot dust emission to the underlying continuum than those in type 2 AGN. Similar results are found for CO absorption-band heads at ∼2.3 μm, which can be diluted by the hot dust emission (Riffel et al. 2009b; Burtscher et al. 2015; Müller-Sánchez et al. 2018b). We find a decrease in the nuclear $EqW_{Br\gamma}$ in 88 per cent (15 objects) of Type 1 AGN, and in 47 per cent (eight objects) of the type 2 AGN, as compared to the extra-nuclear $EqW_{Br\gamma}$ values. The mean values of the ratio between the mean value of the nuclear $EqW_{Br\gamma}$ (computed using an aperture with radius equal to the angular resolution of the data for each galaxy) and the mean extra-nuclear $EqW_{Br\gamma}$ (computed using spaxels at distances larger than the angular resolution) is 1.35 ± 0.27 and 0.58 ± 0.14 for the type 2 and type 1 AGN in our sample, respectively. Considering only the galaxies that show a nuclear decrease in $EqW_{Br\gamma}$, the mean ratios between the nuclear and extra-nuclear $EqW_{Br\gamma}$ are 0.52 ± 0.11 and 0.39 ± 0.07 for type 2 and type 1 AGN, respectively.

The difference in the equivalent widths in type 1 and type 2 AGN can be reconciled with the AGN unification model, as in type 1 AGN we observe directly the contribution of the inner and hotter region of the dusty torus, while in type 2 AGN this structure is not visible in most objects. Smaller $EqW_{Br\gamma}$ values at the nucleus compared to extra-nuclear regions could also be produced if the latter includes a larger contribution of young stellar populations than the former. Our results can be compared to those of Burtscher et al. (2015), who investigated the dilution of the *K*-band CO 2.3 μm absorption feature in a sample of nearby AGN hosts. They computed the intrinsic CO equivalent width (not affected by dilution) and found a wide range of values (from 6 to 14 Å), probably due to differences in the ages of the stellar populations in their sample. Our $EqW_{Br\gamma}$ maps (Figs 2, 3, A1, and A2) also show a wide range of values, which may be due to different stellar populations in the host galaxies. However, Burtscher et al. (2015) found no difference in the intrinsic CO equivalent widths of diluted and undiluted sources (see their Fig. 3), which provides a additional support that the nuclear decrease in $EqW_{Br\gamma}$ in our sample is due to dilution of the line by the AGN continuum.

4.2 The origin of the H_2 emission

The origin of the H_2 near-IR emission lines in active galaxies has been investigated in several theoretical and observational studies (e.g Black & van Dishoeck 1987; Hollenbach & McKee 1989; Draine & Woods 1990; Maloney, Hollenbach & Tielens 1996; Rodríguez-Ardila et al. 2004, 2005; Lamperti et al. 2017), but it is still not clear which is the main excitation mechanism – if

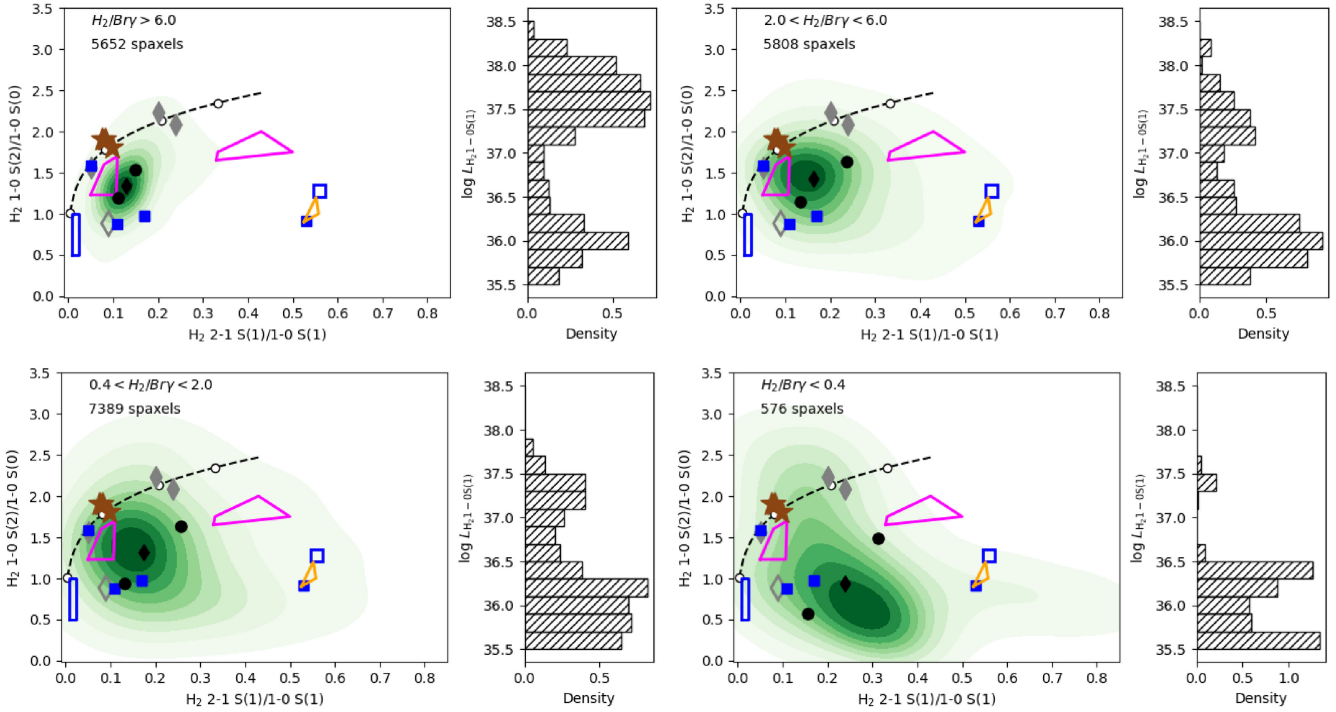

Figure 8. Density plots for the H_2 2–1 S(1)/1–0 S(1) versus 1–0 S(2)/1–0 S(0) diagnostic diagram for spaxels with H_2 2.1218 μm/Brγ > 6.0 (top left), 2.0 <H_2 2.1218 μm/Brγ < 6.0 (top right), 0.4 <H_2 2.1218 μm/Brγ < 2.0 (bottom left), and H_2 2.1218 μm/Brγ < 0.4 (botom right). Black circles in all diagrams correspond to the 25th percentile and 75th percentile of the observed line ratio. Black diamonds represent the median values. The black dashed curve corresponds to the ratios for an isothermal and uniform density gas distribution for temperatures ranging from 1000 (left) to 4000 K (right) – the open circles identify the ratios in steps of 1000 K. The orange polygon represents the region occupied by the non-thermal UV excitation models of Black & van Dishoeck (1987) and the pink polygons cover the region of the photoionization models of Dors et al. (2012). The blue rectangle covers the locus of the thermal UV excitation models of Sternberg & Dalgarno (1989), as computed by Mouri (1994) for gas densities (n_t) of 10^5 and 10^6 cm^{-3} and UV scaling factors relative to the local interstellar radiation field χ from 10^2 to 10^4. The filled blue squares are the UV thermal models from Davies et al. (2003) for $10^3 < n_t < 10^6$ cm^{-3} and $10^2 < \chi < 10^5$, while the open blue square is from Sternberg & Dalgarno (1989) for $n_t = 10^3$ cm^{-3} and $\chi = 10^2$. The brown stars are from the thermal X-ray models of Draine & Woods (1990), the grey open diamond is from the shock model of Kwan et al. (1977) and the grey filled diamonds represent the shock models from Smith (1995). The AGN photoionization from Riffel et al. (2013a) span a wide range in both axes (0 ≲H_2 2–1 S(1)/1–0 S(1)≲ 0.6 and 0.5 ≲ 1–0 S(2)/1–0 S(0)≲ 2.5) and therefore is not shown in the figure. The right-hand panels show the H_2 2.1218 μm luminosity distributions for the spaxels used in the left-hand panels, in logarithmic units of erg s^{-1}.

there is a dominant – of the H_2 molecule. In summary, three main processes can produce the H_2 emission: (i) fluorescent excitation by the absorption of soft-ultraviolet (UV) photons (912–1108 Å) in the Lyman and Werner bands (Black & van Dishoeck 1987), (ii) excitation by shocks (Hollenbach & McKee 1989), and (iii) excitation by X-ray illumination (Maloney et al. 1996). The first process is usually referred as non-thermal, while the latter two are commonly reported as thermal processes, where the H_2 emitting gas is in local thermodynamic equilibrium (LTE). In some cases, thermal and non-thermal processes are observed simultaneously with the H_2 1–0 transitions in LTE, while the higher energy ones (H_2 2–1 and H_2 3–2) being due to fluorescent excitation of the dense gas (Davies et al. 2003, 2005).

In thermal processes, the rotational and vibrational temperatures are similar, as the gas is in LTE, while for fluorescent excitation the vibrational temperature is high (T_{vib} ∼5000 K) and the rotational temperature is about a tenth of T_{vib}, as the highest energy levels are overpopulated due to non-local UV photons compared to the prediction for a Maxwell–Boltzmann population (Sternberg & Dalgarno 1989; Rodríguez-Ardila et al. 2004). As shown in Table 4, for all galaxies, but NGC 788, the median values of the rotational temperature are larger than 10 per cent of the vibrational temperatures. On average, we find $\langle T_{rot}/T_{vib}\rangle = 0.48 \pm 0.31$. This value is consistent with measurements based on single aperture spectra of AGN (e.g. Rodríguez-Ardila et al. 2005; Riffel et al. 2013a).

The H_2/Brγ line ratio is useful in the investigation of the origin of the H_2 emission. In star-forming regions and starburst galaxies, this ratio is usually smaller than 0.4, while AGN present $0.4 < H_2/Br\gamma < 6.0$ and larger values are usually associated to shocks (Riffel et al. 2013a). We find the median values of H_2/Brγ in our sample are within the range observed in AGN, but there is a trend of higher ratios being observed at larger distances from the nucleus for most galaxies, as seen in Table 3 and Figs 2, 3, A1, and A2. Since the H_2 line intensity generally decreases with distance from the nucleus, an explanation for the higher values of the H_2/Brγ away from the nucleus is that the Brγ decreases faster with radius, i.e. it is enhanced very close around the AGN (excited primarily by the AGN) while the H_2 is excited by processes that operate on more extended spatial scales such as shocks.

In order to further investigate the H_2 emission origin, we construct the H_2 2–1 S(1)/1–0 S(1) versus 1–0 S(2)/1–0 S(0) diagnostic diagrams shown in Fig. 8. The density plots show the observed line ratios for all spaxels where we were able to detect all H_2 emission lines. We separate the data into four diagrams, according to the H_2/Brγ presented in the excitation maps (see Figs 2, 3, A1, and A2): $H_2 > 6.0$ – indicative of shocks (top left panel), $2.0 < H_2/Br\gamma < 6.0$

– high excitation AGN (top right panel), $0.4 < H_2/Br\gamma < 2.0$ – low excitation AGN (bottom left panel), and $H_2/Br\gamma < 0.4$ – typical value of starbursts (bottom right panel). The number of points in each plot is shown in the top left corner of the corresponding panel.

The observed H_2 2–1 S(1)/1–0 S(1) and 1–0 S(2)/1–0 S(0) line ratio distributions for $H_2/Br\gamma > 0.4$ lie close to the region predicted by photoionization (pink polygons) and shock models (grey symbols) suggesting thermal processes dominate the H_2 excitation. This result is in good agreement with previous works using single aperture measurements of the H_2 line fluxes (e.g. Rodríguez-Ardila et al. 2004, 2005; Riffel et al. 2013a). Here, we show not only the nuclear emission originates from thermal processes but that also the emission from locations furthest from the nucleus, as the vast majority (96 per cent) of the spaxels in our sample present $H_2/Br\gamma > 0.4$.

Although the peak of the distributions of H_2 2–1 S(1)/1–0 S(1) and 1–0 S(2)/1–0 S(0) is observed nearly at the same location for both spaxels with $0.4 < H_2/Br\gamma < 2.0$, $2.0 < H_2/Br\gamma < 6.0$, and $H_2/Br\gamma > 6.0$, the distributions are distinct. For the $0.4 < H_2/Br\gamma < 2.0$ (low excitation AGN) and $2.0 < H_2/Br\gamma < 6.0$ (high excitation AGN), the luminosity distribution of the H_2 2.1218 μm is very similar and both H_2 2–1 S(1)/1–0 S(1) and 1–0 S(2)/1–0 S(0) spread over a larger region in the diagnostic diagram. The peak in the diagnostic diagrams lie close to both the photoionization model (pink polygons) and to the UV thermal models (filled blue squares) indicating that heating due to the AGN may be the cause of the gas excitation. Also, the fact that the points on the diagram are not distributed along the isothermal line indicates that the gas is not in LTE. For the typical AGN line ratio, $0.4 < H_2/Br\gamma < 6.0$, the H_2 emission can either be produced by shocks (grey symbols) or by the AGN radiation field.

The $H_2/Br\gamma > 6.0$ shows a more concentrated distribution in the diagnostic diagram and is particularly elongated towards higher values of 1–0 S(2)/1–0 S(0). The H_2 2.1218 μm distribution is concentrated towards higher values, indicating the higher ratios is due to the higher H_2 luminosity. This line ratio is more sensitive to shocks, as seen from the wider range of values predicted by distinct shock models for this ratio than for the 2–1 S(1)/1–0 S(1; Kwan et al. 1977; Smith 1995). Thus, the H_2 emission from locations with $H_2/Br\gamma > 6.0$ likely originates from heating of the gas by shocks, as those produced by AGN winds (e.g. Riffel et al. 2020).

For $H_2/Br\gamma < 0.4$, typical of star-forming regions, the median values of 2–1 S(1)/1–0 S(1) and 1–0 S(2)/1–0 S(0) – 0.39 and 1.09, respectively – are close to the predicted values by the models of Black & van Dishoeck (1987; orange polygon) for fluorescent excitation. The peak of the observed distribution of ratios is shifted to slightly lower values of 2–1 S(1)/1–0 S(1) than predicted by the models, but a large scatter is seen in both axes. This shift can be understood as a contamination of thermal excitation plus the dissociation of part of the H_2 molecules by the AGN radiation field, as seen in some objects (Storchi-Bergmann et al. 2009; Riffel et al. 2010a; Gnilka et al. 2020).

4.3 Mass reservoir in the central region and AGN feeding

The galaxies of our sample present masses of hot molecular gas ranging from a few tens of solar masses to 10^4 $M_\odot$ and of ionized gas in the range $\sim 10^3 - 10^7$ $M_\odot$ within the inner 125 pc radius (Table 4). We can compare these masses with the mass accretion rate ($\dot{m}$) necessary to power the AGN, which is given by:

$$\dot{m} = \frac{L_{\rm bol}}{c^2 \eta}, \quad (5)$$

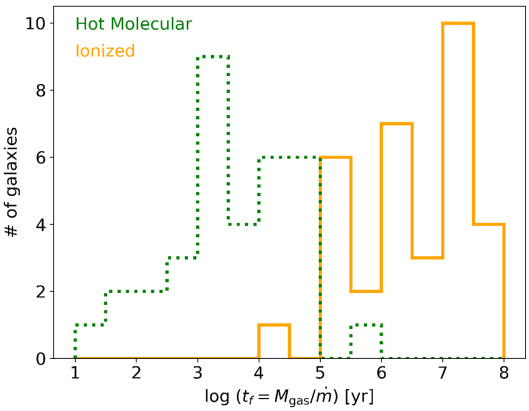

Figure 9. Distribution of the AGN feeding time with the available masses of hot molecular (green) and ionized (orange) hydrogen mass in the inner 125 pc radius.

where c is the light speed, η is the efficiency of conversion of the rest mass energy of the accreted material into radiation assumed to be 0.1 (Frank, King & Raine 2002), and $L_{\rm bol}$ is the AGN bolometric luminosity, which can be estimated from the hard X-ray (14-195 keV) luminosities (L_X) listed in Table 1, by Ichikawa et al. (2017):

$$\log L_{\rm bol} = 0.0378(\log L_X)^2 - 2.03 \log L_X + 61.6. \quad (6)$$

Fig. 9 shows the feeding time ($t_f = M_{\rm gas}/\dot{m}$) distributions for the galaxies computed using the hot molecular and ionized gas masses calculated in the previous sections within the inner 125 pc. We find the mass of ionized gas alone can feed the central AGN for 10^5–10^8 yr at the current accretion rates. The mass of hot molecular gas is on average three orders of magnitude smaller than that of ionized gas. We emphasize that the feeding times estimated above should be treated as an upper limit, as they are based on the total line fluxes and we do not separate the components associated to non-circular motions (e.g. due to inflows and outflows).

The hot molecular and ionized gas masses represent only the 'tip of the iceberg' of the the total gas mass in the centre of galaxies. Dempsey & Zakamska (2018) find the mass of the NLR, measured from emission-line fluxes of the ionized gas, is underestimated because the gas behind the ionization front is invisible in ionized transitions. This gas may be in the molecular phase, dominated by cold molecular gas, and we now know that the mass of cold molecular gas correlates with the H_2 2.1218 μm luminosity – and thus with the hot H_2 mass (Dale et al. 2005; Müller Sánchez et al. 2006; Mazzalay et al. 2013). These studies found that the amount of cold molecular gas is 10^5–10^8 times that of hot H_2. Thus, the cold molecular gas could provide fuel necessary to power the AGN for an activity cycle of 10^5–10^6 yr (e.g. Novak, Ostriker & Ciotti 2011) and still remain available to form new stars in the nuclear region.

5 CONCLUSIONS

We have used Gemini NIFS K-band observations to map the H_2 and $Br\gamma$ emission distribution within the inner 0.04–2 kpc of a sample of 36 active galaxies with $0.001 \lesssim z \lesssim 0.056$ and hard X-ray luminosities in the range $41 \lesssim \log L_X/({\rm erg\,s^{-1}}) \lesssim 45$. The spatial resolutions at the galaxies range from 6 to 250 pc and the field of view covers from the inner 75×75 pc^2 to 3.6×3.6 kpc^2. The main conclusions of this work are:

(i) Extended H_2 2.1218 μm and Brγ emission is observed in 34/36 galaxies of our sample. There is no statistically significant difference between the orientation of the H_2 and Brγ flux distributions relative to the orientation of the major axis of the host galaxy (ΔPA). We find ΔPA larger than 30° in 15 galaxies (42 per cent) for the Brγ and in 16 galaxies (44 per cent) for H_2.

(ii) The H_2 emission is usually more spread over the field of view, while the Brγ shows a more collimated flux distribution in most cases and a steeper flux gradient, decreasing with the distance from the nucleus. We find offsets larger than 30° between the orientations of the H_2 2.1218 μm and Brγ flux distributions in 45 per cent of our sample. On average, the radius that contains 50 per cent of the total H_2 emission is ∼60 per cent larger than that for Brγ.

(iii) We derive the H_2 rotational and vibrational temperatures based on the observed H_2 1-0 S(1) 2.1218 μm/2-1 S(1) 2.2477 μm and 1-0 S(2) 2.0338 μm/1-0S(0) 2.2235 μm line ratios. The median values are in the ranges 2100–4300 K and 450–1900 K for the vibrational and rotational temperatures, respectively, with the mean ratio between the two of 0.43 ± 0.15, indicating dominant thermal excitation for the gas.

(iv) Type 1 and type 2 AGN show similar emission-line flux distributions, ratios, H_2 excitation temperatures and gas masses, supporting the AGN unification scenario.

(v) Type 1 and 2 AGN differ only in their nuclear Brγ equivalent widths, which are smaller in type 1 AGN due to larger contributions of hot dust emission to the *K*-band continuum in type 1 nuclei.

(vi) The distribution of points in the H_2 2–1 S(1)/1–0 S(1) versus 1–0 S(2)/1–0 S(0) diagram in regions with H_2/Brγ > 0.4 (96 per cent of all spaxels with flux measurements) are consistent with predictions of photoionization and shock models, confirming that the main excitation mechanism of the H_2 molecule are thermal processes, not only at the nucleus but also in the extranuclear regions.

(vii) The gas thermal excitation usually increases outwards with H_2/Brγ values increasing from <2 in the nucleus to values up to six outwards.

(viii) In locations with H_2/Brγ >6.0, the most likely H_2 excitation mechanism are shocks, as indicated by the H_2 2–1 S(1)/1–0 S(1) and 1–0 S(2)/1–0 S(0) line ratios. This is observed mostly in locations away from the nucleus, for ∼40 per cent of the galaxies.

(ix) Most of the regions with H_2/Brγ < 0.4 (4 per cent of the spaxels with flux measurements) are consistent with fluorescent excitation of the H_2, but dissociation of the H_2 molecule by the AGN radiation cannot be ruled out in galaxies with small H_2/Brγ nuclear values. This is observed in ∼25 per cent of the sample.

(x) The mass of hot molecular and ionized gas in the inner 125 pc radius are in the ranges 10^1-10^4 $M_\odot$ and 10^4-10^6 $M_\odot$, respectively. The masses computed for the whole NIFS field of view are about one order of magnitude larger.

(xi) The mass of ionized gas within the inner 125 pc radius alone is more than enough to power the AGN in our sample for a duty cycle of 10^6 yr at their current accretion rates.

ACKNOWLEDGEMENTS

RAR acknowledges financial support from Conselho Nacional de Desenvolvimento Científico e Tecnológico (CNPq – 202582/2018-3, 304927/2017-1, 400352/2016-8, and 312036/2019-1) and Fundação de Amparo à pesquisa do Estado do Rio Grande do Sul (FAPERGS – 17/2551-0001144-9 and 16/2551-0000251-7). RR thanks CNPq, CAPES and FAPERGS for financial support. MB thanks the financial support from Coordenação de Aperfeiçoamento de Pessoal de Nível Superior - Brasil (CAPES) - Finance Code 001. NZD acknowledges partial support from FONDECYT through project 3190769. Based on observations obtained at the Gemini Observatory, which is operated by the Association of Universities for Research in Astronomy, Inc., under a cooperative agreement with the NSF on behalf of the Gemini partnership: the National Science Foundation (United States), National Research Council (Canada), CONICYT (Chile), Ministerio de Ciencia, Tecnología e Innovación Productiva (Argentina), Ministério da Ciência, Tecnologia e Inovação (Brazil), and Korea Astronomy and Space Science Institute (Republic of Korea). This research has made use of NASA's Astrophysics Data System Bibliographic Services. This research has made use of the NASA/IPAC Extragalactic Database (NED), which is operated by the Jet Propulsion Laboratory, California Institute of Technology, under contract with the National Aeronautics and Space Administration.

DATA AVAILABILITY

Most of the data used in this paper are available in the Gemini Science Archive at https://archive.gemini.edu/searchform with the project codes listed in Table 1. Processed datacubes used will be shared on reasonable request to the corresponding author.

REFERENCES

Antonucci R., 1993, ARA&A, 31, 473
Audibert A., Riffel R., Sales D. A., Pastoriza M. G., Ruschel-Dutra D., 2017, MNRAS, 464, 2139
Barbosa F. K. B., Storchi-Bergmann T., McGregor P., Vale T. B., Rogemar Riffel A., 2014, MNRAS, 445, 2353
Baron D., Netzer H., 2019, MNRAS, 486, 4290
Barth A. J., Filippenko A. V., Moran E. C., 1999, ApJ, 515, L61
Black J. H., van Dishoeck E. F., 1987, ApJ, 322, 412
Brum C., Riffel R. A., Storchi-Bergmann T., Robinson A., Schnorr Müller A., Lena D., 2017, MNRAS, 469, 3405
Brum C. et al., 2019, MNRAS, 486, 691
Burtscher L. et al., 2015, A&A, 578, A47
Caglar T. et al., 2020, A&A, 634, A114
Colina L. et al., 2015, A&A, 578, A48
Daddi E. et al., 2010, ApJ, 713, 686
Dahmer-Hahn L. G. et al., 2019a, MNRAS, 482, 5211
Dahmer-Hahn L. G. et al., 2019b, MNRAS, 489, 5653
Dale D. A., Sheth K., Helou G., Regan M. W., Hüttemeister S., 2005, AJ, 129, 2197
Davies R. I., Sternberg A., Lehnert M., Tacconi-Garman L. E., 2003, ApJ, 597, 907
Davies R. I., Sternberg A., Lehnert M. D., Tacconi-Garman L. E., 2005, ApJ, 633, 105
Davies R. I., Maciejewski W., Hicks E. K. S., Tacconi L. J., Genzel R., Engel H., 2009, ApJ, 702, 114
Davies R. I. et al., 2014, ApJ, 792, 101
Davies R. I. et al., 2015, ApJ, 806, 127
Davies R. et al., 2020, MNRAS, 498, 4150
de Vaucouleurs G., de Vaucouleurs A., Corwin H. G. J., Buta R. J., Paturel G., Fouque P., 1991, Third Reference Catalogue of Bright Galaxies. Springer-Verlag, New York
Dempsey R., Zakamska N. L., 2018, MNRAS, 477, 4615
Diniz M. R., Riffel R. A., Storchi-Bergmann T., Winge C., 2015, MNRAS, 453, 1727
Diniz M. R., Riffel R. A., Dors O. L., 2018, Res. Notes Am. Astron. Soc., 2, 3
Dors O. L. J., Storchi-Bergmann T., Riffel R. A., Schimdt A. A., 2008, A&A, 482, 59
Dors O. L. J., Riffel R. A., Cardaci M. V., Hägele G. F., Krabbe Á. C., Pérez-Montero E., Rodrigues I., 2012, MNRAS, 422, 252
Dors O. L., Cardaci M. V., Hägele G. F., Krabbe Â. C., 2014, MNRAS, 443, 1291
Dors O. L., Maiolino R., Cardaci M. V., Hägele G. F., Krabbe A. C., Pérez-Montero E., Armah M., 2020, MNRAS, 496, 3209

Draine B. T., Woods D. T., 1990, ApJ, 363, 464
Drehmer D. A., Storchi-Bergmann T., Ferrari F., Cappellari M., Riffel R. A., 2015, MNRAS, 450, 128
Dumont A., Seth A. C., Strader J., Greene J. E., Burtscher L., Neumayer N., 2020, ApJ, 888, 19
Durré M., Mould J., 2014, ApJ, 784, 79
Durré M., Mould J., 2018, ApJ, 867, 149
Elitzur M., 2012, ApJ, 747, L33
Elitzur M., Ho L. C., Trump J. R., 2014, MNRAS, 438, 3340
Fazeli N., Eckart A., Busch G., Yttergren M., Combes F., Misquitta P., Straubmeier C., 2020, A&A, 638, A36
Fischer T. C. et al., 2017, ApJ, 834, 30
Frank J., King A., Raine D. J., 2002, Accretion Power in Astrophysics, 3rd edn. Cambridge Univ. Press, Cambridge
Freitas I. C. et al., 2018, MNRAS, 476, 2760
Genzel R. et al., 2010, MNRAS, 407, 2091
Gnilka C. L. et al., 2020, ApJ, 893, 80
Gonzalez Delgado R. M., Perez E., 1997, MNRAS, 284, 931
Harrison C. M., 2017, Nat. Astron., 1, 0165
Harrison C. M., Costa T., Tadhunter C. N., Flütsch A., Kakkad D., Perna M., Vietri G., 2018, Nat. Astron., 2, 198
Heckman T. M., 1980, A&A, 500, 187
Heckman T. M., Best P. N., 2014, ARA&A, 52, 589
Hicks E. K. S., Davies R. I., Malkan M. A., Genzel R., Tacconi L. J., Müller Sánchez F., Sternberg A., 2009, ApJ, 696, 448
Hollenbach D., McKee C. F., 1989, ApJ, 342, 306
Hopkins P. F., Quataert E., 2010, MNRAS, 407, 1529
Ho L. C., Filippenko A. V., Sargent W. L. W., Peng C. Y., 1997, ApJS, 112, 391
Husemann B. et al., 2019, A&A, 627, A53
Ichikawa K., Ricci C., Ueda Y., Matsuoka K., Toba Y., Kawamuro T., Trakhtenbrot B., Koss M. J., 2017, ApJ, 835, 74
Ilha G. d. S., Bianchin M., Riffel R. A., 2016, Ap&SS, 361, 178
Jin Y. et al., 2016, MNRAS, 463, 913
Kakkad D. et al., 2018, A&A, 618, A6
Keel W. C., 1990, AJ, 100, 356
Kormendy J., Ho L. C., 2013, ARA&A, 51, 511
Kwan J. H., Gatley I., Merrill K. M., Probst R., Weintraub D. A., 1977, ApJ, 216, 713
Lamperti I. et al., 2017, MNRAS, 467, 540
Lin M.-Y. et al., 2018, MNRAS, 473, 4582
Liu G., Zakamska N. L., Greene J. E., Nesvadba N. P. H., Liu X., 2013, MNRAS, 436, 2576
Lutz D., Sturm E., Genzel R., Spoon H. W. W., Moorwood A. F. M., Netzer H., Sternberg A., 2003, A&A, 409, 867
McGregor P. J. et al., 2003, in Iye M., Moorwood A. F. M., eds, SPIE Conf. Ser. Vol. 4841, Instrument Design and Performance for Optical/Infrared Ground-based Telescopes. SPIE, Bellingham, p. 1581
Maloney P. R., Hollenbach D. J., Tielens A. G. G. M., 1996, ApJ, 466, 561
May D., Steiner J. E., 2017, MNRAS, 469, 994
May D., Steiner J. E., Menezes R. B., Williams D. R. A., Wang J., 2020, MNRAS, 496, 1488
Mazzalay X. et al., 2013, MNRAS, 428, 2389
Mouri H., 1994, ApJ, 427, 777
Müller Sánchez F., Davies R. I., Eisenhauer F., Tacconi L. J., Genzel R., Sternberg A., 2006, A&A, 454, 481
Müller-Sánchez F., Nevin R., Comerford J. M., Davies R. I., Privon G. C., Treister E., 2018a, Nature, 556, 345
Müller-Sánchez F., Hicks E. K. S., Malkan M., Davies R., Yu P. C., Shaver S., Davis B., 2018b, ApJ, 858, 48
Novak G. S., Ostriker J. P., Ciotti L., 2011, ApJ, 737, 26
Oh K. et al., 2018, ApJS, 235, 4
Osterbrock D. E., Ferland G. J., 2006, Astrophysics of Gaseous Nebulae and Active Galactic Nuclei, 2nd edn. University Science Books, Mill Valley, CA
Pasquali A., Gallagher J. S., de Grijs R., 2004, A&A, 415, 103
Paturel G., Petit C., Prugniel P., Theureau G., Rousseau J., Brouty M., Dubois P., Cambrésy L., 2003, A&A, 412, 45
Prieto M. A., Mezcua M., Fernández-Ontiveros J. A., Schartmann M., 2014, MNRAS, 442, 2145
Puxley P. J., Hawarden T. G., Mountain C. M., 1990, ApJ, 364, 77
Ramos Almeida C. et al., 2011, ApJ, 731, 92
Reunanen J., Kotilainen J. K., Prieto M. A., 2002, MNRAS, 331, 154
Ricci T. V., Steiner J. E., Menezes R. B., 2014, MNRAS, 440, 2419
Riffel R. A., 2020, MNRAS, 494, 2004
Riffel R., Rodríguez-Ardila A., Pastoriza M. G., 2006, A&A, 457, 61
Riffel R. A., Storchi-Bergmann T., Winge C., McGregor P. J., Beck T., Schmitt H., 2008, MNRAS, 385, 1129
Riffel R. A., Storchi-Bergmann T., Dors O. L., Winge C., 2009a, MNRAS, 393, 783
Riffel R., Pastoriza M. G., Rodríguez-Ardila A., Bonatto C., 2009b, MNRAS, 400, 273
Riffel R. A., Storchi-Bergmann T., McGregor P. J., 2009c, ApJ, 698, 1767
Riffel R. A., Storchi-Bergmann T., Nagar N. M., 2010a, MNRAS, 404, 166
Riffel R. A., Storchi-Bergmann T., Riffel R., Pastoriza M. G., 2010b, ApJ, 713, 469
Riffel R., Rodríguez-Ardila A., Aleman I., Brotherton M. S., Pastoriza M. G., Bonatto C., Dors O. L., 2013a, MNRAS, 430, 2002
Riffel R. A., Storchi-Bergmann T., Winge C., 2013b, MNRAS, 430, 2249
Riffel R. A., Vale T. B., Storchi-Bergmann T., McGregor P. J., 2014, MNRAS, 442, 656
Riffel R. A., Storchi-Bergmann T., Riffel R., Dahmer-Hahn L. G., Diniz M. R., Schönell A. J., Dametto N. Z., 2017, MNRAS, 470, 992
Riffel R. A. et al., 2018, MNRAS, 474, 1373
Riffel R. A., Storchi-Bergmann T., Zakamska N. L., Riffel R., 2020, MNRAS, 496, 4857
Riffel R. A., Bianchin M., Riffel R., Storchi-Bergmann T., Schönell A. J., Dahmer-Hahn L. G., Dametto N. Z., Diniz M. R., 2021, MNRAS, 503, 5161
Rodríguez-Ardila A., Pastoriza M. G., Viegas S., Sigut T. A. A., Pradhan A. K., 2004, A&A, 425, 457
Rodríguez-Ardila A., Riffel R., Pastoriza M. G., 2005, MNRAS, 364, 1041
Rosario D. J., Togi A., Burtscher L., Davies R. I., Shimizu T. T., Lutz D., 2019, ApJ, 875, L8
Ruschel-Dutra D., 2020, danielrd6/ifscube v1.0. Zenodo. Available at: https://doi.org/10.5281/zenodo.3945237
Sargent M. T. et al., 2014, ApJ, 793, 19
Scharwächter J., McGregor P. J., Dopita M. A., Beck T. L., 2013, MNRAS, 429, 2315
Schinnerer E., Eckart A., Tacconi L. J., 2000, ApJ, 533, 826
Schönell A. J., Riffel R. A., Storchi-Bergmann T., Winge C., 2014, MNRAS, 445, 414
Schönell A. J. J., Storchi-Bergmann T., Riffel R. A., Riffel R., 2017, MNRAS, 464, 1771
Schönell A. J., Storchi-Bergmann T., Riffel R. A., Riffel R., Bianchin M., Dahmer-Hahn L. G., Diniz M. R., Dametto N. Z., 2019, MNRAS, 485, 2054
Scoville N. Z., Hall D. N. B., Ridgway S. T., Kleinmann S. G., 1982, ApJ, 253, 136
Shimizu T. T. et al., 2019, MNRAS, 490, 5860
Silverman J. D. et al., 2015, ApJ, 812, L23
Smith M. D., 1995, A&A, 296, 789
Sternberg A., Dalgarno A., 1989, ApJ, 338, 197
Storchi-Bergmann T., Schnorr-Müller A., 2019, Nat. Astron., 3, 48
Storchi-Bergmann T., McGregor P. J., Riffel R. A., Simões Lopes R., Beck T., Dopita M., 2009, MNRAS, 394, 1148
Turner J., Kirby-Docken K., Dalgarno A., 1977, ApJS, 35, 281
Urry C. M., Padovani P., 1995, PASP, 107, 803
Villarroel B., Korn A. J., 2014, Nat. Phys., 10, 417
Wilgenbus D., Cabrit S., Pineau des Forêts G., Flower D. R., 2000, A&A, 356, 1010

APPENDIX A: GEMINI NIFS MEASUREMENTS

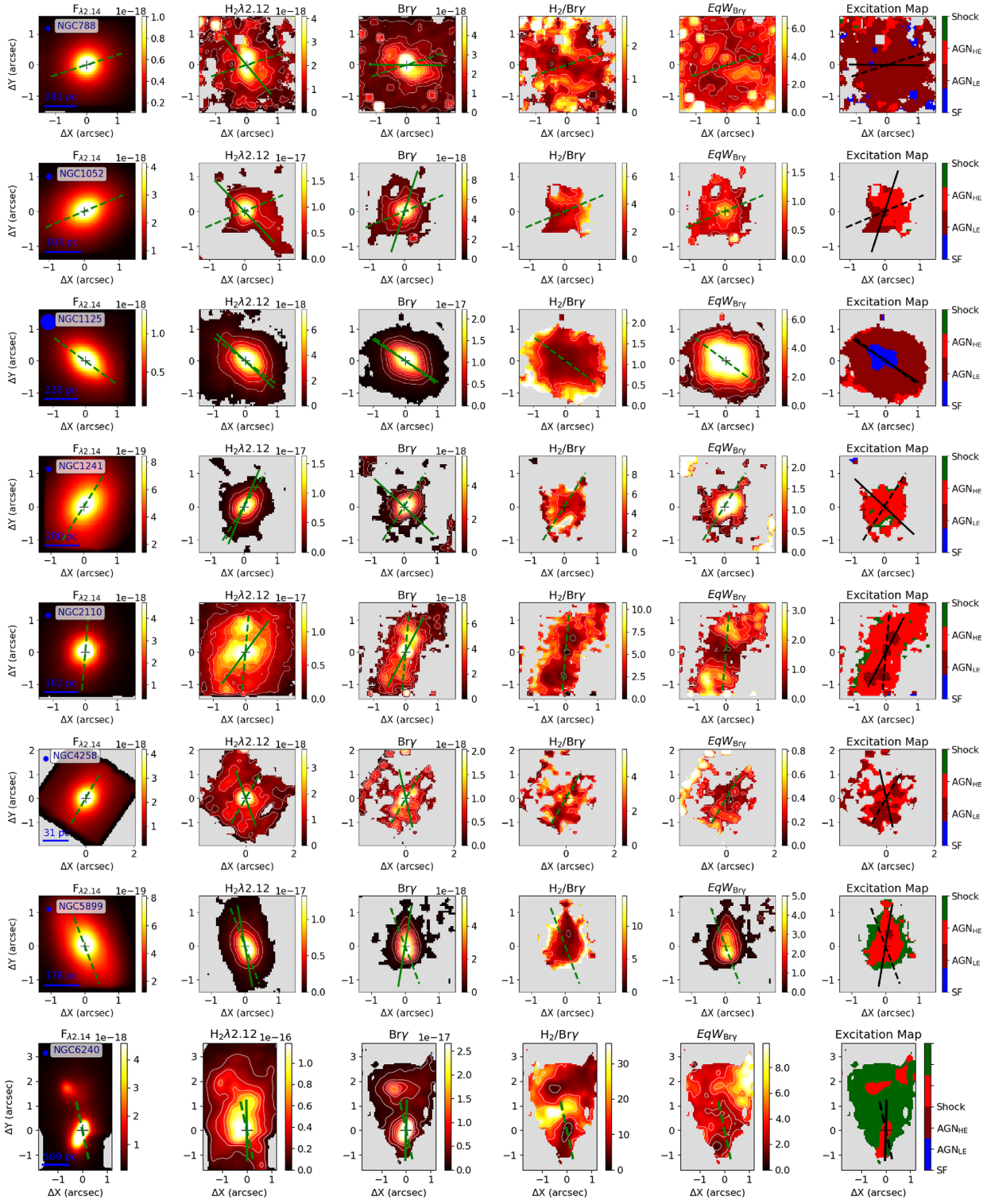

Figure A1. Maps for type 2 AGN. From left to right: *K*-band continuum obtained within a spectral window of 100 Å centred at 2.14 μm, H$_2$ 2.1218 μm flux distribution, Brγ flux distribution, H$_2$/Brγ ratio map, Brγ equivalent width map, and excitation map. The colour bars show the continuum in units of erg s^{-1} cm^{-2} Å^{-1} spaxel^{-1}, the emission-line fluxes in erg s^{-1} cm^{-2} spaxel^{-1}, and the Brγ equivalent width in Å. The excitation map identifies the regions with typical H_2/Brγ values for star-forming galaxies (SF: H$_2$/Brγ < 0.4), AGN with low excitation (AGN$_{LE}$: $0.4 \leq$ H$_2$/Brγ < 2), and high excitation (AGN$_{HE}$: $2 \leq$ H$_2$/Brγ < 6) and higher line ratios, usually observed in shock dominated objects (Shock: H$_2$/Brγ > 6). In each row, the name of the galaxy is identified in the continuum image, the filled circle corresponds to the angular resolution of the data, the spatial scale is shown in the bottom-left corner of the continuum image, and the cross marks the position of the peak of the continuum emission. The dashed line indicates the orientation of the galaxy major axis obtained from the Hyperleda database. The continuous line on the flux maps shows the orientation of the emission-line flux distributions. The continuous line on the excitation map shows the orientation of the Brγ emission. The grey regions indicate locations where the emission lines are not detected within 2σ above the continuum noise. For all galaxies, north is up and east is to the left.

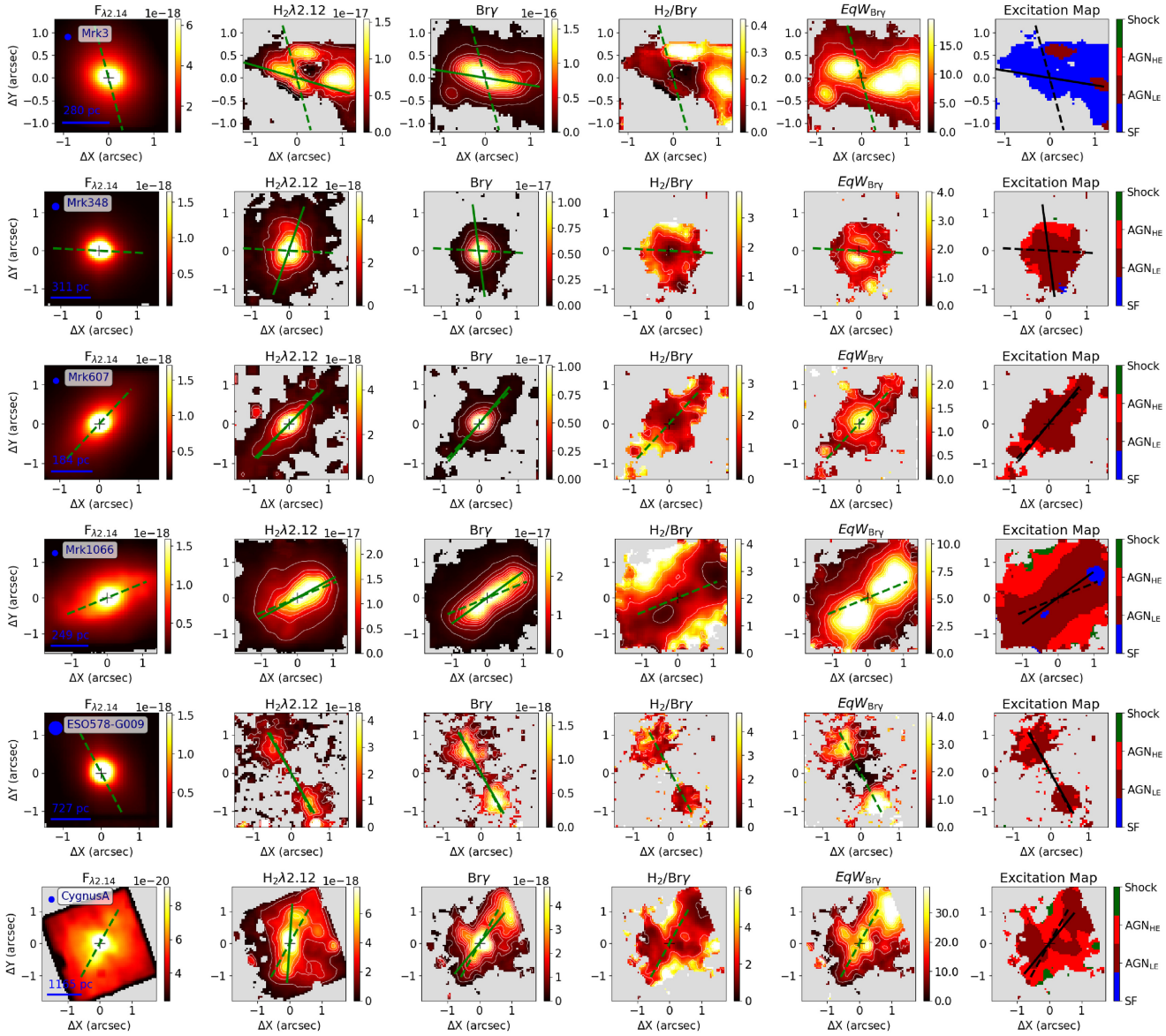

Figure A1 - *continued*

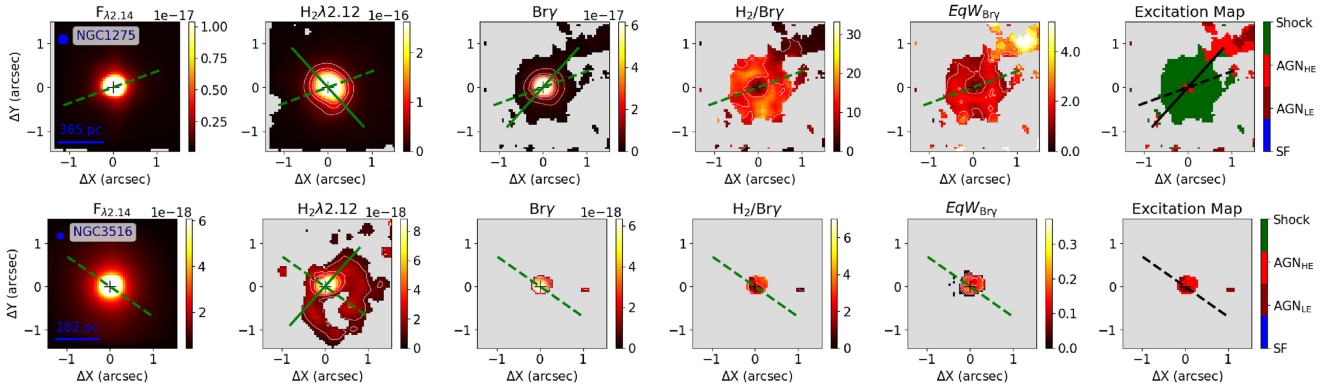

Figure A2. Maps for type 1 AGN. Same as Fig. A1, but for type 1 AGN.

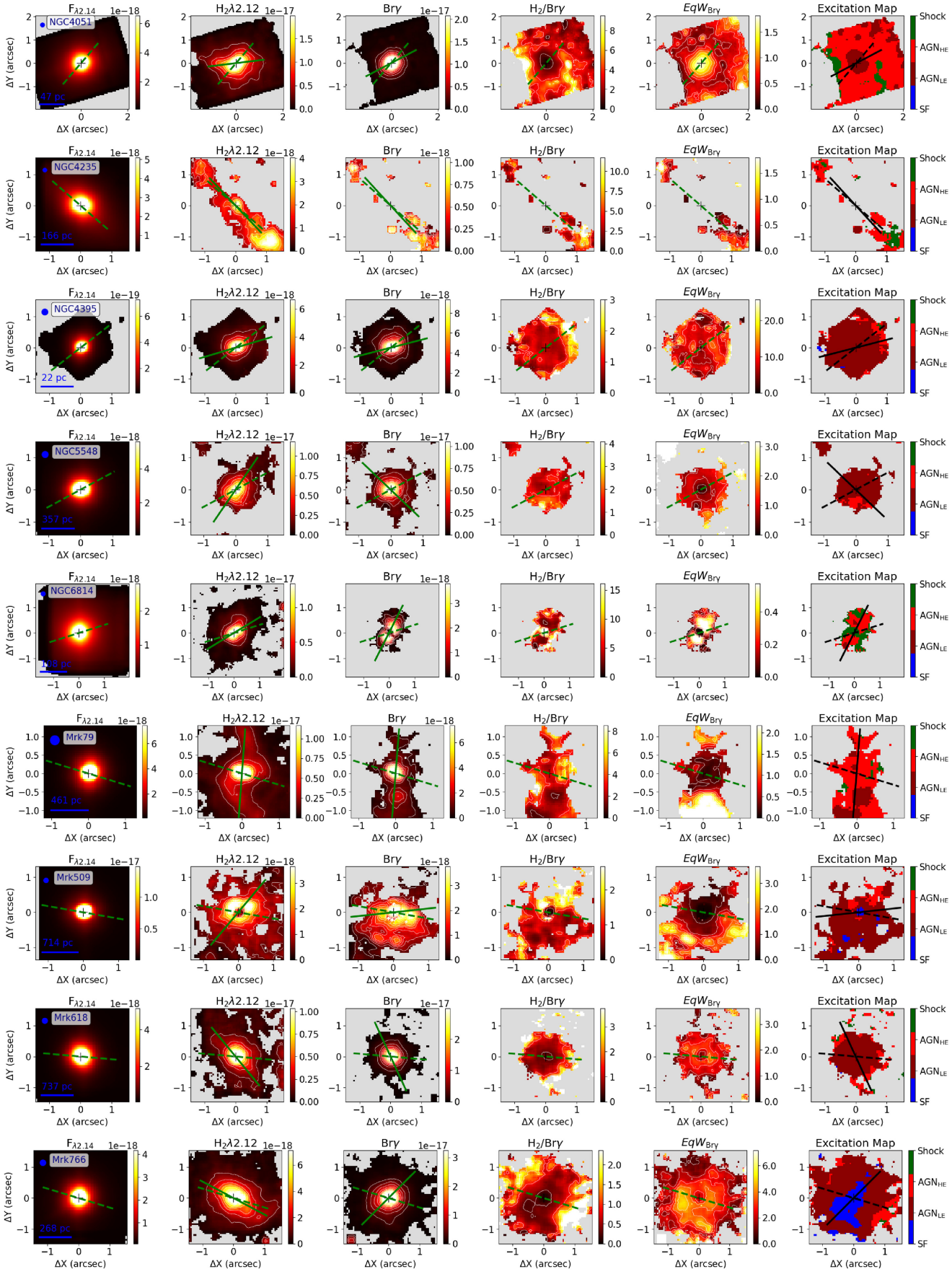

Figure A2 - *continued*

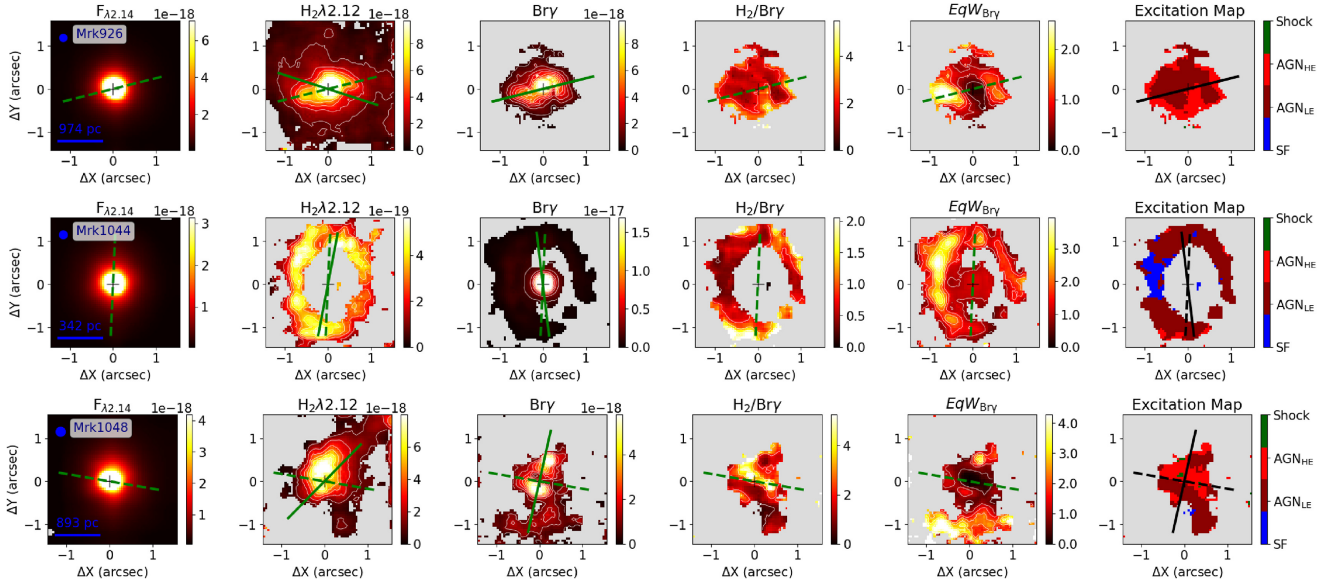

Figure A2 - *continued*

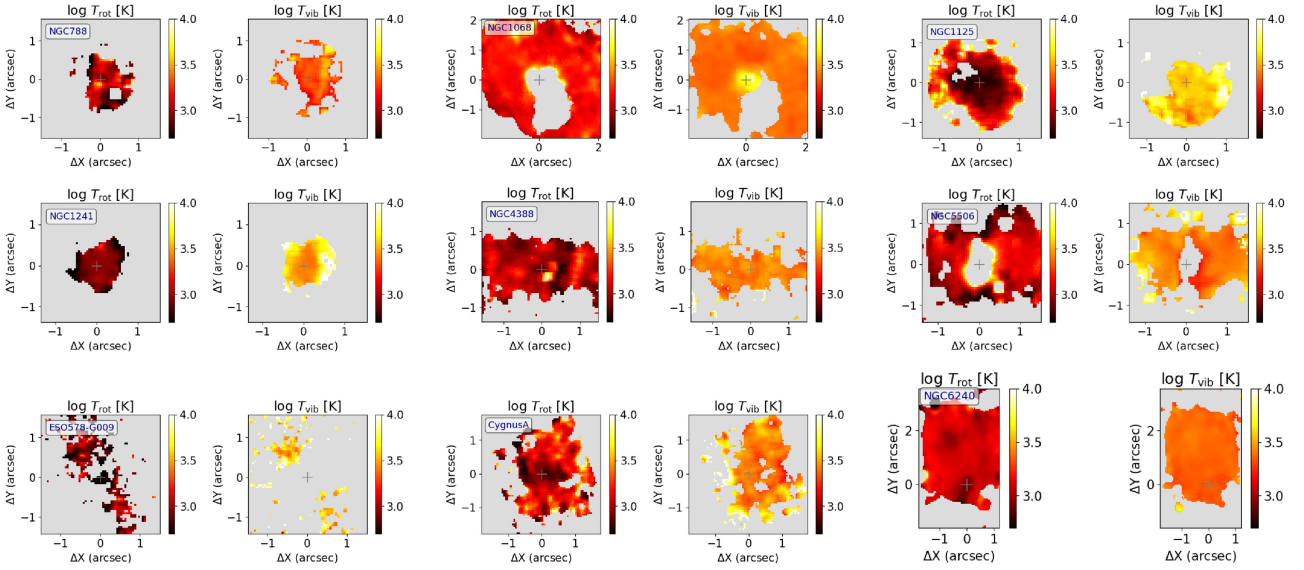

Figure A3. H_2 rotational and vibrational temperatures for type 2 in our sample calculated according to equations (3 and 4). The grey regions indicate locations where at least one of the H_2 emission lines is not detected within 2σ above the continuum noise. The colorbar shows the temperatures in logarithmic scale in units of K.

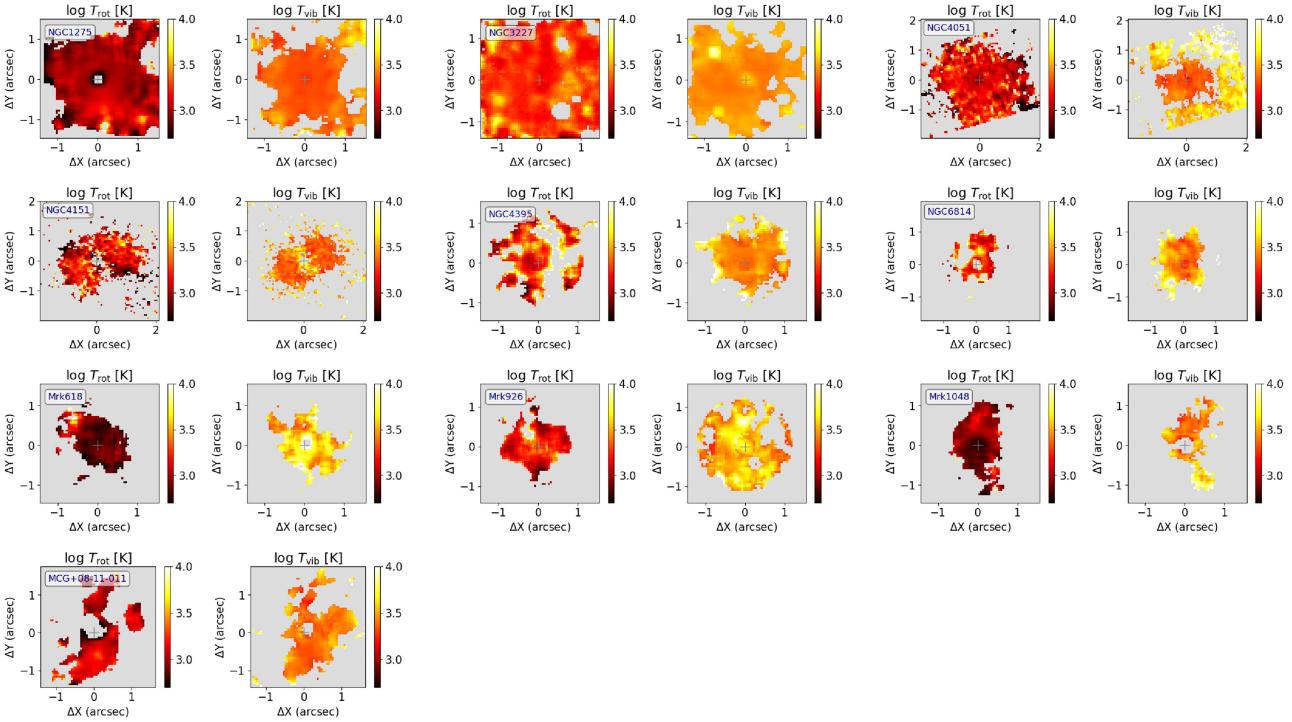

Figure A4. Same as A3, but for type 1 AGN.

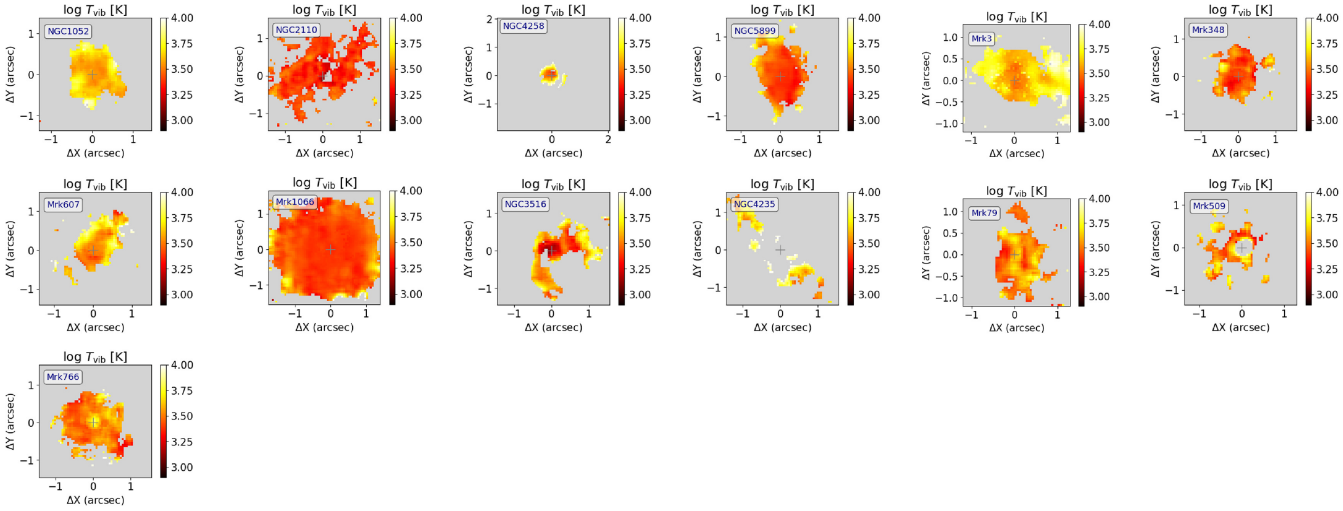

Figure A5. H_2 vibrational for objects where the H_2 1–0 S(2) line is not detected.

This paper has been typeset from a TEX/LATEX file prepared by the author.